An exceptional infrared transient from a star engulfing a planet

Kishalay De (kde1@mit.edu)
Massachusetts Institute of Technology
Morgan MacLeod
Center for Astrophysics | Harvard & Smithsonian
Viraj Karambelkar
Caltech
Jacob Jencson
Department of Physics and Astronomy, Johns Hopkins University
Deepto Chakrabarty
MIT
Charlie Conroy
Harvard University https://orcid.org/0000-0002-1590-8551
Richard Dekany
California Institute of Technology https://orcid.org/0000-0002-5884-7867
Anna-Christina Eilers
MIT Kavli Institute for Astrophysics and Space Research
Matthew Graham
California Institute of Technology https://orcid.org/0000-0002-3168-0139
Lynne Hillenbrand
Caltech
Erin Kara
Massachusetts Institute of Technology https://orcid.org/0000-0003-0172-0854
Mansi Kasliwal
California Institute of Technology
Shri Kulkarni
Caltech Optical Observatories
Ryan Lau
NSF's National Optical-Infrared Astronomy Research Laboratory
Abraham Loeb
Harvard University https://orcid.org/0000-0003-4330-287X
Frank Masci
Caltech https://orcid.org/0000-0002-8532-9395
Michael Medford

University of California Berkeley
Aaron Meisner
NSF's National Optical-Infrared Astronomy Research Laboratory
Nimesh Patel
Harvard-Smithsonian Center for Astrophysics
Luis Quiroga-Nunez
Department of Aerospace, Physics and Space Sciences, Florida Institute of Technology
Reed Riddle
California Institute of Technology https://orcid.org/0000-0002-0387-370X
Benjamin Rusholme
Caltech https://orcid.org/0000-0001-7648-4142
Robert Simcoe
MIT
Lorant Sjouwerman
National Radio Astronomy Observatory
Richard Teague
Center for Astrophysics|Harvard & Smithsonian
Andrew Vanderburg
MIT https://orcid.org/0000-0001-7246-5438

Physical Sciences - Article

Keywords:

Posted Date: October 4th, 2022

DOI: https://doi.org/10.21203/rs.3.rs-2117913/v1

An exceptional infrared transient from a star engulfing a planet

Kishalay De[1,2] *, Morgan MacLeod[3], Viraj Karambelkar[4], Jacob E. Jencson[5], Deepto Chakrabarty[1], Charlie Conroy[3], Richard Dekany[6], Anna-Christina Eilers[1,7], Matthew J. Graham[4], Lynne A. Hillenbrand[4], Erin Kara[1], Mansi M. Kasliwal[4], S. R. Kulkarni[4], Ryan M. Lau[8], Abraham Loeb[3,9], Frank Masci[10], Michael S. Medford[11,12], Aaron M. Meisner[8], Nimesh Patel[3], Luis Henry Quiroga-Nuñez[13], Reed L. Riddle[6], Ben Rusholme[10], Robert Simcoe[1], Loránt O. Sjouwerman[14], Richard Teague[3,15] and Andrew Vanderburg[1]

[1]*Kavli Institute for Astrophysics and Space Research, Massachusetts Institute of Technology, Cambridge, MA 02139, USA*

[2]*NASA Einstein Fellow*

[3]*Center for Astrophysics — Harvard & Smithsonian 60 Garden Street, MS-16, Cambridge, MA 02138, USA*

[4]*Cahill Center for Astrophysics, California Institute of Technology, 1200 E. California Boulevard, Pasadena, CA 91125, USA*

[5]*Department of Physics and Astronomy, Johns Hopkins University, Baltimore, MD 21218, USA*

[6]*Caltech Optical Observatories, California Institute of Technology, Pasadena, CA 91125, USA*

[7]*NASA Hubble Fellow*

[8]*NSF's National Optical-Infrared Astronomy Research Laboratory, 950 N. Cherry Ave., Tucson, AZ 85719, USA*

[9]*Black Hole Initiative, Harvard University, Cambridge, MA 02138, USA*

[10]*IPAC, California Institute of Technology, 1200 E. California Blvd, Pasadena, CA 91125, USA*

[11]*Department of Astronomy, University of California, Berkeley, Berkeley, CA 94720, USA*

[12]*Lawrence Berkeley National Laboratory, 1 Cyclotron Rd., Berkeley, CA 94720, USA*

[13]*Department of Aerospace, Physics and Space Sciences, Florida Institute of Technology, 150 W University Blvd, Melbourne, 32901, FL, USA*

[14]*National Radio Astronomy Observatory, Array Operations Center, Socorro, NM 87801, USA*

[15]*Department of Earth, Atmospheric, and Planetary Sciences, Massachusetts Institute of Technology, Cambridge, MA 02139, USA*

It is well known that planets with short orbital periods ($\lesssim 10$ days) are common around stars like the Sun[1–3]. Stars expand as they evolve, and thus we expect their close planetary companions to be engulfed[4–6]. However, this phase has never been directly observed. Here, we present the discovery of ZTF SLRN-2020, a short-lived optical outburst in the Galactic disk accompanied by bright and long-lived infrared emission. The resulting light curve and spectra share striking similarities with those of red novae[7,8] – a class of eruptions now confirmed[9] to arise from mergers of binary stars. Its exceptionally low optical luminosity ($\approx 10^{35}$ erg s^{-1}) and radiated energy ($\approx 6.5 \times 10^{41}$ erg) point to the engulfment of a planet (of $1 - 10$ Jupiter masses) by its Sun-like host star. We estimate the Galactic rate of such Sub-luminous Red Novae (SLRNe) to be $\sim 0.1-$few yr^{-1}. Future Galactic plane surveys are well-poised to routinely identify them, revealing the demographics of planetary engulfment and the ultimate fate of planets in the inner Solar System.

Using data from the Zwicky Transient Facility (ZTF) time domain survey[10], we searched for slowly evolving outbursts near the Galactic plane (Methods). We identified a transient optical source named ZTF 20aazusyv (hereafter ZTF SLRN-2020) that exhibited a fast rise from quiescence to peak outburst flux in ≈ 10 days, subsequently fading by $\approx 10\times$ over six months (Figure 1). The long optical outburst duration together with its faint peak flux distinguishes it from common Galactic plane transients resulting from white dwarfs with close binary companions (the 'dwarf' and 'classical' novae[11]). The transient also exhibits a mid-IR brightening starting ≈ 7 months prior to the optical outburst, together with bright mid-infrared (IR) emission ($> 50\times$ brighter than the optical r-band at ≈ 4 months after optical peak) that lasted for $\gtrsim 15$ months. No X-ray emission was detected in follow-up observations during the outburst using the Swift telescope[12], ruling out an unstable disk accretion episode around a neutron star or black hole[13] (Methods).

The bright mid-IR emission during the outburst is suggestive of emission from a warm dust shell surrounding the stellar photosphere. We model the optical to mid-IR spectral energy distribution (SED; Methods) at ≈ 120 days after the optical peak. The analysis reveal a relatively hot inner photosphere (≈ 9000 K) surrounded by a warm dust shell with temperature ≈ 1000 K, located behind a dust visual extinction column of $A_V \approx 3.6$ mag (Figure 2). Using the 90% confidence interval on the foreground extinction together with three-dimensional Galactic dust distribution maps (Methods), we infer the source to be located at a distance of 2 to 7 kpc. A joint analysis of the overlap between the different dust maps suggests a likely distance of ≈ 4 kpc (Methods). Performing the same analysis at ≈ 320 days after peak, we find the SED to have predominantly shifted into the IR bands caused by an increase in the dust optical depth, that can be attributed to the formation of $\approx 10^{-6}\,M_\odot$ of dust (for a distance of 4 kpc).

Using the best estimate for the foreground extinction, we construct a bolometric luminosity light curve for the outburst (Figure 2; Methods). The light curve is characterized by an initial plateau at a luminosity of $\approx 10^{35} \times (d/4\,\mathrm{kpc})^2\,\mathrm{erg\,s^{-1}}$ lasting ≈ 25 days (Methods) before fading by a factor of 5 over the next ≈ 100 days. The effective temperature of the photosphere stays constant at $\approx (6-7) \times 10^3$ K during the plateau phase, presumably regulated by the recombination temperature of hydrogen[14], before fading and cooling to $\approx 5 \times 10^3$ K. The total radiated energy is $\approx 6.5 \times 10^{41} (d/4\,\mathrm{kpc})^2$ erg over the first ≈ 150 days.

On UT 2020 November 20, we obtained an optical spectrum of the transient using the Keck-I telescope. The spectrum (Figure 3) exhibits a nearly featureless red continuum containing only atomic (Na, Ba, H and Mg) and molecular absorption features (VO and TiO). The lack of such atomic emission lines during the outburst is inconsistent with common Galactic plane transients such as accretion events in young stars[15] as well as accretion/thermonuclear outbursts in dwarf and classical novae[16,17], where hot gas produces emission lines due to atomic recombination and ions (Methods). Instead, the molecular features are suggestive of a cool outer photosphere consistent with a M4-III type giant star and effective temperature of ≈ 3600 K (Methods). Contemporaneous near-infrared (NIR) spectra (Figure 3) obtained with the Palomar 200-inch telescope show only broad molecular absorption bands from H_2O and likely TiO, VO and CO, consistent with a M7-III type giant possessing an extended, cool envelope (Methods). Late-time NIR spectra (Figure 3) obtained ≈ 700 days after the optical peak with the Magellan Baade and Keck-II telescopes show only a relatively featureless continuum with broad H_2O absorption.

The distinctively cool molecular spectroscopic features together with the substantial reddening of the SED during the outburst are reminiscent of the class of 'red novae'[9, 18–21]. Direct photometric observations of the binary orbital decay prior to the red nova V1309 Sco[9] provide strong evidence for these events to be associated with catastrophic mergers of binary stars. As the primary star engulfs its companion, a powerful outflow is launched from the binary system that gradually cools and powers a 'plateau' in the light curve of the optical transient via recombination of hydrogen[7, 22]. Subsequently, the expanding envelope cools and forms dust leading to the emergence of a photosphere dominated by molecular absorption and a luminous, long-lived infrared transient[23–25].

The photometric and spectroscopic properties of ZTF SLRN-2020 share striking similarities with both Galactic and extragalactic red novae (Methods). Yet, its remarkably low luminosity, even if placed on the far side of the Galactic disk ($\lesssim$ few$\times 10^{36}$ erg s^{-1}), makes it exceptional in the population of red novae that reach the Eddington luminosity of the primary stars ($\approx 10^{38}$ erg s^{-1} for a $1\,M_{\odot}$ star). We show ZTF SLRN-2020 in the phase space of luminosity and timescales (Figure 4; Methods) for red novae together with analytical contours for the mass and velocity of ejecta in models of stellar mergers[8]. The extremely low luminosity is reasonably explained by only $\sim 10^{-5} - 10^{-4}\,M_{\odot}$ of hydrogen launched in the outflow[8]. The small ejected mass is consistent with the non-detection of radio molecular line emission in follow-up observations with the Submillimeter Array (SMA) and Very Large Array (VLA; Methods).

Using a high spatial resolution image obtained with the Gemini-South telescope ≈ 2 years after the outburst peak, we identify a faint progenitor source (Methods) in archival NIR images from the United Kingdom Infrared Telescope (UKIRT) Galactic plane survey[26]. Although limited by the photometric errors, its brightness and colors are consistent with a $\approx 0.8 - 1.5\,\mathrm{M}_\odot$ star on the main sequence or early in the sub-giant branch (radius $1 - 4\,\mathrm{R}_\odot$). The infrared progenitor is thus similar to the Sun, and to the primary star of V1309 Sco, which was a merger event involving a low-mass $q = 0.1$ companion, where q is the companion to primary mass ratio[9,27–30].

We draw constraints on the mass of the merging object from both the light curve and pre-outburst detections. ZTF SLRN-2020's ejecta mass and radiated energy are both $\sim 10^3\times$ lower than that of V1309 Sco (Figure 4), implying a merger with a very low mass companion of $\approx 0.1{-}1 M_J$. In their evolution towards coalescence, merging systems lose mass to their circumbinary environments, mediating the angular momentum loss that drives their orbital decay [28,30–32]. We compare the pre-outburst limits and detections to these models (Figure 4). The pre-outburst dust model that best matches the data has $q = 10^{-2}$ or a companion mass of $10 M_J$ (Methods). Therefore all our estimates squarely point to a close (< 1 d orbital period) substellar companion to the primary star, plausibly a Jupiter-like planet strikingly similar to known systems[33].

The overall duration of the light curve suggests a mass ejection velocity of roughly 30 km s^{-1} (Figure 4), which is substantially lower than the stellar escape velocity. We can unify these estimates with our theoretical understanding of how planetary engulfment might affect a host star. In particular, the smaller the engulfed companion, the less dramatic the disturbance to the primary star, and the smaller fraction of material that is expected to be ejected at high enough velocities to become unbound[34–36]. The short-lived ≈ 25 d plateau phase in ZTF SLRN-2020 may be powered by the ejection and unbinding of a small amount ($\lesssim 10^{-4} M_{\odot}$) of mass at velocities approaching the stellar escape velocity ($\sim 100\,\mathrm{km\,s^{-1}}$; Figure 4). The radius of ZTF SLRN-2020 (Figure 2) remains roughly constant at $\approx 3 \times 10^{11} \times (d/4\,\mathrm{kpc})$ cm during the plateau and recedes during the fading phase, similar to that expected for the gravitational contraction of a merger remnant[23]. These features suggest that the late-time decay over the next ≈ 100 d is powered by hydrodynamic and thermal readjustment of the star following the ingestion of its planetary companion.

Our interpretation of ZTF SLRN-2020 as the engulfment event of a planetary mass object by a Sun-like star provides evidence for a missing link in our understanding of the evolution and final fates of planetary systems. It has been long known that the population of gas giants in short orbital periods ('hot Jupiters'[1–3,37]) have sufficiently low orbital angular momentum such that they are unstable to tidal dissipation and are bound to merge with their host stars[38–42]. This is consistent with the lack of old planetary systems with short orbital periods[43,44] as well as the dearth of close planets around sub-giant stars[45–47]. Therefore, the observations reported here offer the first direct insight into the effect of planetary engulfment on their host stars to interpret common indirect techniques used to infer past planetary engulfment via its effects on the long-term stellar luminosity[6,48], chemical enrichment[49–53], and stellar rotation[54–58]. With empirical and theoretical rate predictions ranging from 0.1 to few yr^{-1} (Methods) for similar 'sub-luminous red novae' (SLRNe), upcoming combined optical and infrared surveys of the Galactic plane may reveal many similar events, probing the demographics of planetary engulfment and testing theories of the co-evolution of stars and their planetary systems.

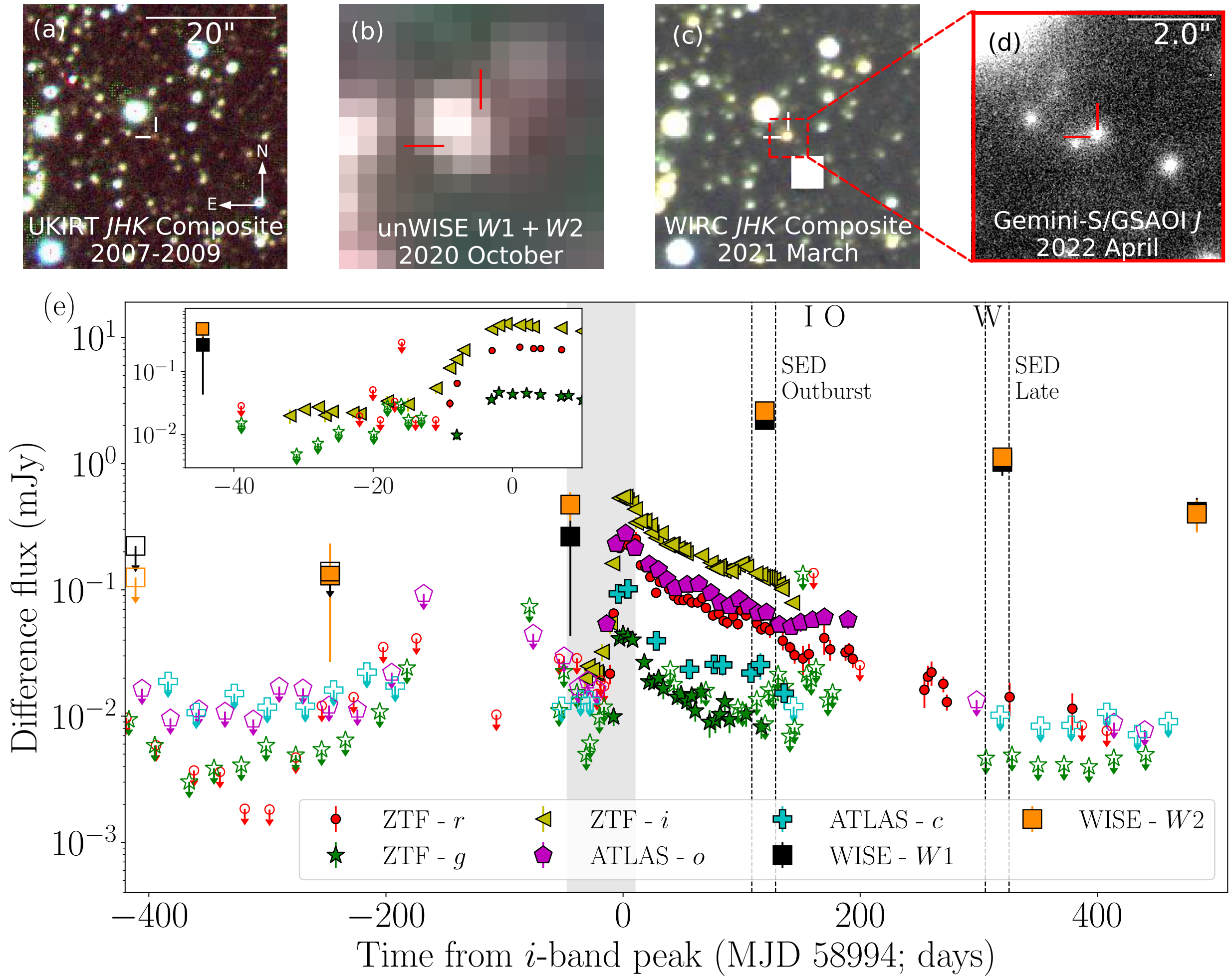

Figure 1: **The discovery location and multi-color light curves of ZTF SLRN-2020**. (a) A faint progenitor identified in archival NIR images from the UKIRT Galactic Plane Survey, (b) the mid-IR transient source detected in NEOWISE images from 2020 , (c) a NIR composite follow-up image (the white square masks out a nearby region with a detector artifact) of the transient during 2021 (Panels (a)-(c) have identical spatial scales) and (d) a zoomed-in high spatial resolution image of the IR remnant in 2022. (e) Multi-color light curves of the outburst from the ZTF[10], ATLAS[59] and NEOWISE[60] surveys (as indicated in the legend). Upper limits are shown as symbols with downward arrows. I and O indicate the times of the NIR and optical spectroscopy of the transient, while W shows the epoch of the P200 NIR imaging. The vertical dashed lines show the time ranges used to perform SED modeling during the outburst in 2020 (SED Outburst) and after the optical transient had faded away in 2021 (SED Late). The inset shows a zoom-in of the early time light curve (shaded in grey in the main panel), showing faint i-band precursor emission and detection of mid-IR emission prior to the onset of the optical outburst.

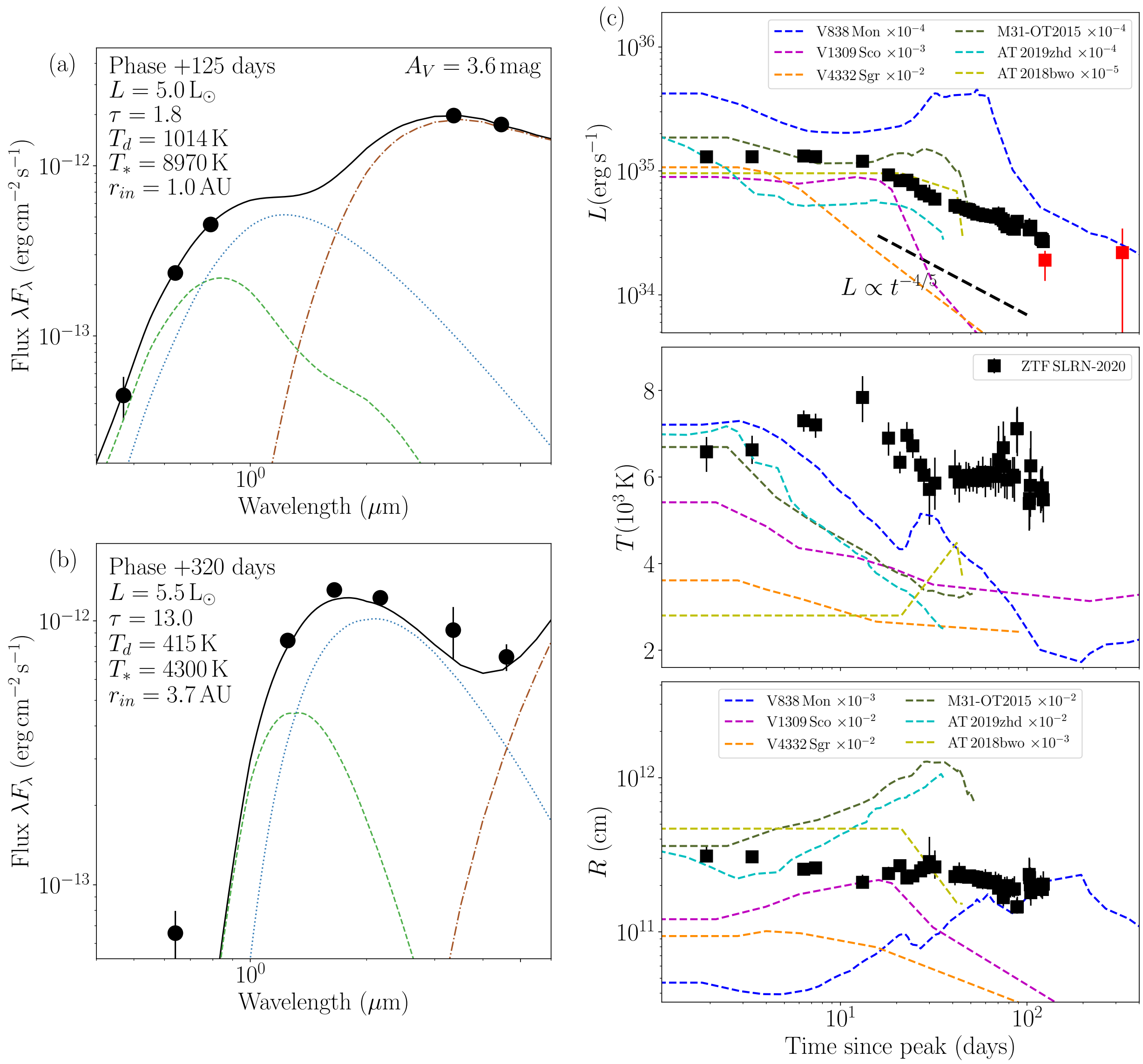

Figure 2: **Spectral energy distribution evolution and bolometric light curve of ZTF SLRN-2020.** (a) Best-fit model (parameters are shown) for the SED of ZTF SLRN-2020 (shown as black circles) at $\approx$ 125 days after outburst peak. The black solid lines show the total flux, the brown dot-dashed lines show the dust emission, while the green dashed and blue dotted lines show the scattered and attenuated stellar emission respectively. (b) Same as (a) but for $\approx$ 320 days after outburst peak. (c) The bolometric luminosity (top), temperature (middle) and radius (bottom) evolution of ZTF SLRN-2020 for an estimated distance of 4 kpc and a foreground interstellar extinction of $A_V = 3.6$ mag. The red squares in the top panel show the luminosity estimated from the two epochs of `DUSTY` modeling. For comparison, we also show the evolution of these parameters for previous red novae, as well as the $L \propto t^{-4/5}$ luminosity decay expected for a merger remnant. The radius and luminosity of archival events have been scaled as indicated.

1. Udry, S. & Santos, N. C. Statistical Properties of Exoplanets. ARA&A **45**, 397–439 (2007).

2. Winn, J. N. & Fabrycky, D. C. The Occurrence and Architecture of Exoplanetary Systems. ARA&A **53**, 409–447 (2015). 1410.4199.

3. Dawson, R. I. & Johnson, J. A. Origins of Hot Jupiters. ARA&A **56**, 175–221 (2018). 1801.06117.

4. Metzger, B. D., Giannios, D. & Spiegel, D. S. Optical and X-ray transients from planet-star mergers. MNRAS **425**, 2778–2798 (2012). 1204.0796.

5. MacLeod, M., Cantiello, M. & Soares-Furtado, M. Planetary Engulfment in the Hertzsprung-Russell Diagram. ApJ **853**, L1 (2018). 1801.04274.

6. Stephan, A. P., Naoz, S., Gaudi, B. S. & Salas, J. M. Eating Planets for Lunch and Dinner: Signatures of Planet Consumption by Evolving Stars. ApJ **889**, 45 (2020). 1909.05259.

7. Ivanova, N., Justham, S., Avendano Nandez, J. L. & Lombardi, J. C. Identification of the Long-Sought Common-Envelope Events. *Science* **339**, 433 (2013). 1301.5897.

8. Matsumoto, T. & Metzger, B. D. Light Curve Model for Luminous Red Novae and Inferences about the Ejecta of Stellar Mergers. *arXiv e-prints* arXiv:2202.10478 (2022). 2202.10478.

9. Tylenda, R. *et al.* V1309 Scorpii: merger of a contact binary. A&A **528**, A114 (2011). 1012.0163.

10. Bellm, E. C. *et al.* The Zwicky Transient Facility: System Overview, Performance, and First Results. PASP **131**, 018002 (2019). 1902.01932.

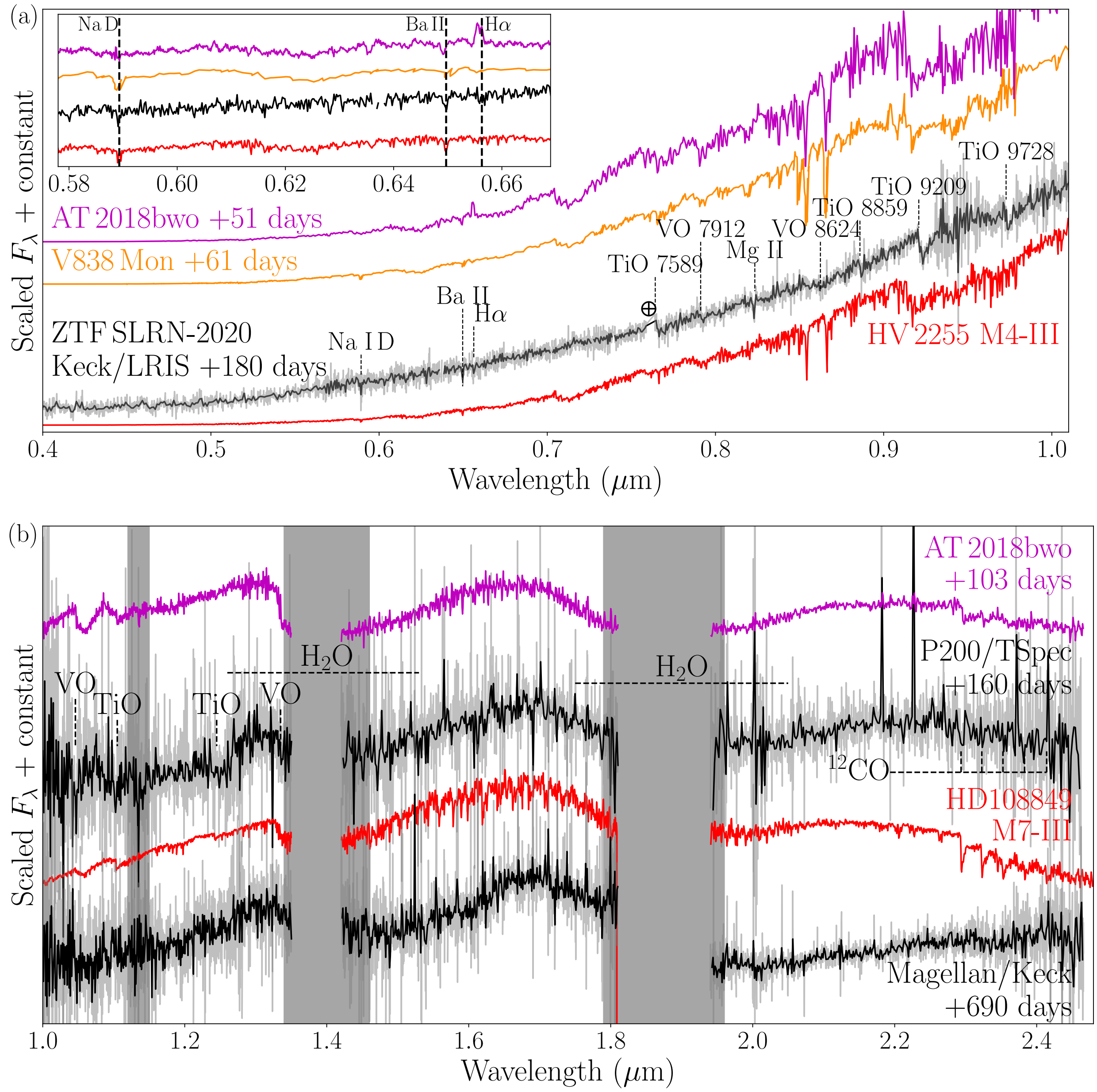

Figure 3: **Optical and infrared spectra of ZTF SLRN-2020**. (a) Optical spectrum of the outburst (black) obtained ≈ 180 days after peak. The spectrum shows clear atomic and molecular absorption features, similar to the M4-III type giant HV 2255. For comparison, late-time optical spectra of a previous Galactic red nova (V838 Mon; in orange) and an extragalactic Luminous Red Nova (AT 2018bwo; in magenta) are shown after applying the inferred foreground extinction[61]. The inset shows a zoom-in of the spectra around the region of the Na D, Hα and Ba II atomic lines. (b) The NIR spectrum of ZTF SLRN-2020 (black) at $\approx +160$ days and $\approx +690$ days after optical peak, showing clear broad molecular absorption features of H_2O, TiO, VO and likely CO, similar to the M7-III giant HD 108849 (shown in red). Similar features are also seen in the NIR spectra of the previously known extragalactic red nova AT 2018bwo (shown in magenta).

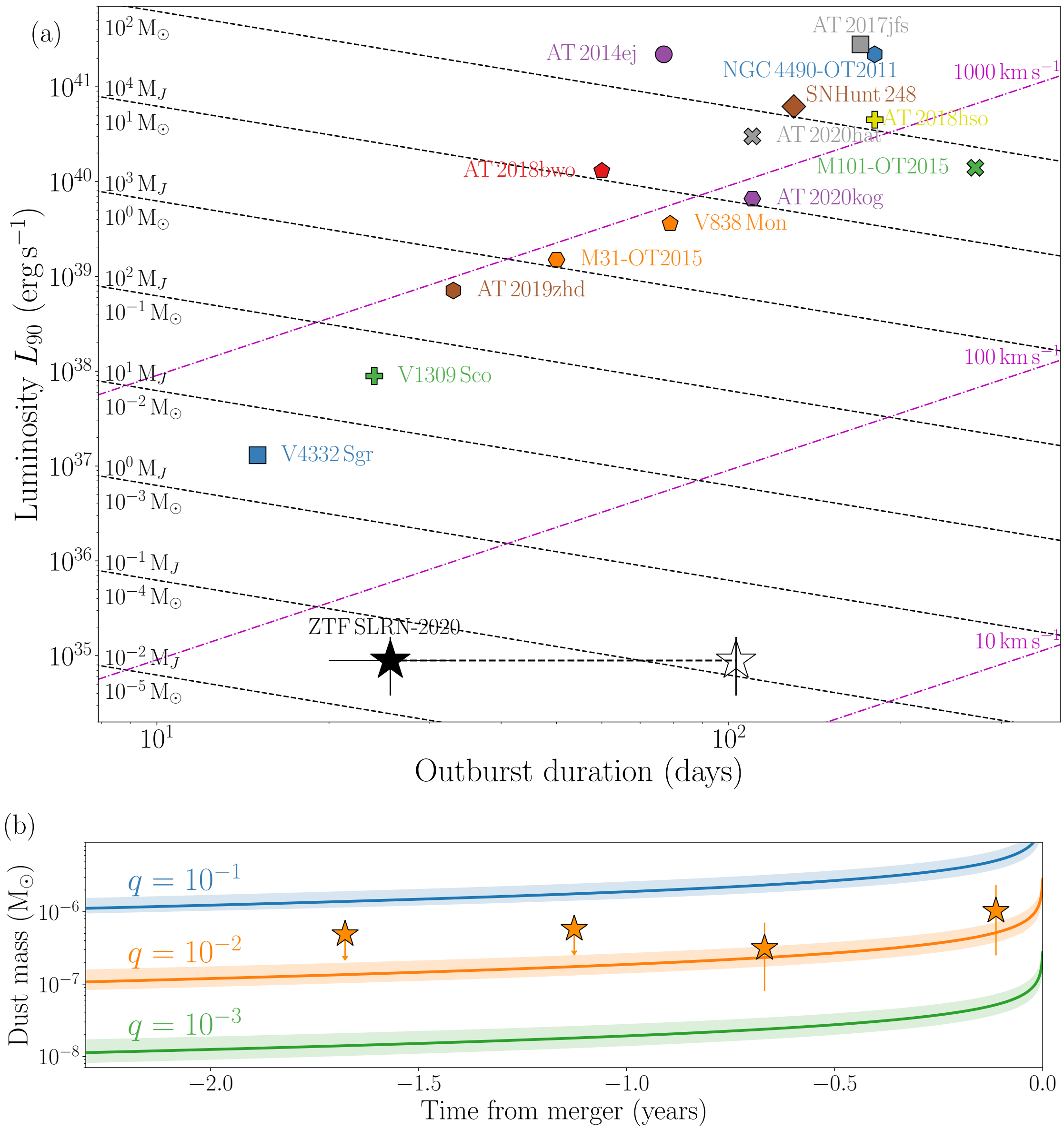

Figure 4: **Comparison of the ZTF SLRN-2020 outburst to the phase space of luminosity (L_{90}) and timescales (t_{90}) for previously known red novae.** (a) Contours show inferred ejecta physical parameters[8] – ejecta mass in units of solar and Jupiter mass on the left axis, and outflow velocity in units of km s^{-1} shown in magenta on the right axis. The solid and hollow star show ZTF SLRN-2020 via its light curve plateau duration and time taken to release 90% of the total radiated energy respectively (Methods).The inferred ejecta mass of ZTF SLRN-2020 is a hundred times lower than any other known red nova, and the characteristic velocities are also nearly an order of magnitude lower. (b) Comparison of the pre-outburst dust mass estimated from the precursor mid-IR emission of ZTF SLRN-2020 (shown as stars) to models of pre-coalescence mass loss for a $1\,M_\odot$ star evolving off the main-sequence with binary mass ratio $q = 10^{-3} - 10^{-1}$. The solid lines correspond to an initial radius of $2\,R_\odot$, while shaded region shows variations for radii of $1 - 4\,R_\odot$.

11. Kawash, A. *et al.* Classical Novae Masquerading as Dwarf Novae? Outburst Properties of Cataclysmic Variables with ASAS-SN. ApJ **910**, 120 (2021). 2101.12239.

12. Gehrels, N. *et al.* The Swift Gamma-Ray Burst Mission. ApJ **611**, 1005–1020 (2004). astro-ph/0405233.

13. Corral-Santana, J. M. *et al.* BlackCAT: A catalogue of stellar-mass black holes in X-ray transients. A&A **587**, A61 (2016). 1510.08869.

14. Popov, D. V. An Analytical Model for the Plateau Stage of Type II Supernovae. ApJ **414**, 712 (1993).

15. Hartmann, L. & Kenyon, S. J. The FU Orionis Phenomenon. ARA&A **34**, 207–240 (1996).

16. Warner, B. *Cataclysmic variable stars*, vol. 28 (1995).

17. Starrfield, S., Iliadis, C. & Hix, W. R. The Thermonuclear Runaway and the Classical Nova Outburst. PASP **128**, 051001 (2016). 1605.04294.

18. Rich, R. M., Mould, J., Picard, A., Frogel, J. A. & Davies, R. Luminous M Giants in the Bulge of M31. ApJ **341**, L51 (1989).

19. Martini, P. *et al.* Nova Sagittarii 1994 1 (V4332 Sagittarii): The Discovery and Evolution of an Unusual Luminous Red Variable Star. AJ **118**, 1034–1042 (1999). astro-ph/9905016.

20. Munari, U. *et al.* The mysterious eruption of V838 Mon. A&A **389**, L51–L56 (2002). astro-ph/0205288.

21. Tylenda, R. *et al.* OGLE-2002-BLG-360: from a gravitational microlensing candidate to an overlooked red transient. A&A **555**, A16 (2013). `1304.1694`.

22. Ivanova, N. *et al.* Common envelope evolution: where we stand and how we can move forward. A&A Rev. **21**, 59 (2013). `1209.4302`.

23. Tylenda, R., Crause, L. A., Górny, S. K. & Schmidt, M. R. V4332 Sagittarii revisited. A&A **439**, 651–661 (2005). `astro-ph/0412205`.

24. Loebman, S. R. *et al.* The Continued Optical to Mid-Infrared Evolution of V838 Monocerotis. AJ **149**, 17 (2015). `1409.2513`.

25. Tylenda, R. & Kamiński, T. Evolution of the stellar-merger red nova V1309 Scorpii: Spectral energy distribution analysis. A&A **592**, A134 (2016). `1606.09426`.

26. Lawrence, A. *et al.* The UKIRT Infrared Deep Sky Survey (UKIDSS). MNRAS **379**, 1599–1617 (2007). `astro-ph/0604426`.

27. Nandez, J. L. A., Ivanova, N. & Lombardi, J., J. C. V1309 Sco—Understanding a Merger. ApJ **786**, 39 (2014). `1311.6522`.

28. Pejcha, O. Burying a Binary: Dynamical Mass Loss and a Continuous Optically thick Outflow Explain the Candidate Stellar Merger V1309 Scorpii. ApJ **788**, 22 (2014). `1307.4088`.

29. Zhu, L.-Y., Zhao, E.-G. & Zhou, X. A low-mass-ratio and deep contact binary as the progenitor of the merger V1309 Sco. *Research in Astronomy and Astrophysics* **16**, 68 (2016). `1611.04699`.

30. Pejcha, O., Metzger, B. D., Tyles, J. G. & Tomida, K. Pre-explosion Spiral Mass Loss of a Binary Star Merger. ApJ **850**, 59 (2017). 1710.02533.

31. MacLeod, M. *et al.* Lessons from the Onset of a Common Envelope Episode: the Remarkable M31 2015 Luminous Red Nova Outburst. ApJ **835**, 282 (2017). 1605.01493.

32. MacLeod, M. & Loeb, A. Runaway Coalescence of Pre-common-envelope Stellar Binaries. ApJ **893**, 106 (2020). 1912.05545.

33. Hellier, C. *et al.* An orbital period of 0.94days for the hot-Jupiter planet WASP-18b. Nature **460**, 1098–1100 (2009).

34. Staff, J. E., De Marco, O., Wood, P., Galaviz, P. & Passy, J.-C. Hydrodynamic simulations of the interaction between giant stars and planets. MNRAS **458**, 832–844 (2016). 1602.03130.

35. MacLeod, M., Ostriker, E. C. & Stone, J. M. Bound Outflows, Unbound Ejecta, and the Shaping of Bipolar Remnants during Stellar Coalescence. ApJ **868**, 136 (2018). 1808.05950.

36. MacLeod, M. & Loeb, A. Pre-common-envelope Mass Loss from Coalescing Binary Systems. ApJ **895**, 29 (2020). 2003.01123.

37. Wright, J. T. *et al.* The Frequency of Hot Jupiters Orbiting nearby Solar-type Stars. ApJ **753**, 160 (2012). 1205.2273.

38. Hut, P. Tidal evolution in close binary systems. A&A **99**, 126–140 (1981).

39. Mardling, R. A. & Lin, D. N. C. Calculating the Tidal, Spin, and Dynamical Evolution of Extrasolar Planetary Systems. ApJ **573**, 829–844 (2002).

40. Levrard, B., Winisdoerffer, C. & Chabrier, G. Falling Transiting Extrasolar Giant Planets. ApJ **692**, L9–L13 (2009). 0901.2048.

41. Patra, K. C. *et al.* The Continuing Search for Evidence of Tidal Orbital Decay of Hot Jupiters. AJ **159**, 150 (2020). 2002.02606.

42. Yee, S. W. *et al.* The Orbit of WASP-12b Is Decaying. ApJ **888**, L5 (2020). 1911.09131.

43. Hamer, J. H. & Schlaufman, K. C. Hot Jupiters Are Destroyed by Tides While Their Host Stars Are on the Main Sequence. AJ **158**, 190 (2019). 1908.06998.

44. Hamer, J. H. & Schlaufman, K. C. Ultra-short-period Planets Are Stable against Tidal Inspiral. AJ **160**, 138 (2020). 2007.10944.

45. Johnson, J. A. *et al.* Retired A Stars and Their Companions: Exoplanets Orbiting Three Intermediate-Mass Subgiants. ApJ **665**, 785–793 (2007). 0704.2455.

46. Schlaufman, K. C. & Winn, J. N. Evidence for the Tidal Destruction of Hot Jupiters by Subgiant Stars. ApJ **772**, 143 (2013). 1306.0567.

47. Grunblatt, S. K. *et al.* Giant Planet Occurrence within 0.2 au of Low-luminosity Red Giant Branch Stars with K2. AJ **158**, 227 (2019). 1910.05346.

48. Metzger, B. D., Shen, K. J. & Stone, N. Secular dimming of KIC 8462852 following its consumption of a planet. MNRAS **468**, 4399–4407 (2017). 1612.07332.

49. Sandquist, E., Taam, R. E., Lin, D. N. C. & Burkert, A. Planet Consumption and Stellar Metallicity Enhancements. ApJ **506**, L65–L68 (1998). astro-ph/9808128.

50. Siess, L. & Livio, M. The accretion of brown dwarfs and planets by giant stars - I. Asymptotic giant branch stars. MNRAS **304**, 925–937 (1999). astro-ph/9812220.

51. Israelian, G., Santos, N. C., Mayor, M. & Rebolo, R. Lithium in stars with exoplanets. A&A **414**, 601–611 (2004). astro-ph/0310378.

52. Soares-Furtado, M., Cantiello, M., MacLeod, M. & Ness, M. K. Lithium Enrichment Signatures of Planetary Engulfment Events in Evolved Stars. AJ **162**, 273 (2021). 2002.05275.

53. Spina, L. *et al.* Chemical evidence for planetary ingestion in a quarter of Sun-like stars. *Nature Astronomy* **5**, 1163–1169 (2021). 2108.12040.

54. Soker, N. Can Planets Influence the Horizontal Branch Morphology? AJ **116**, 1308–1313 (1998). astro-ph/9803223.

55. Carlberg, J. K., Majewski, S. R. & Arras, P. The Role of Planet Accretion in Creating the Next Generation of Red Giant Rapid Rotators. ApJ **700**, 832–843 (2009). 0906.1587.

56. Zhang, M. & Penev, K. Stars Get Dizzy After Lunch. ApJ **787**, 131 (2014). 1404.4365.

57. Aguilera-Gómez, C., Chanamé, J., Pinsonneault, M. H. & Carlberg, J. K. On Lithium-rich Red Giants. I. Engulfment of Substellar Companions. ApJ **829**, 127 (2016). 1605.05332.

58. Qureshi, A., Naoz, S. & Shkolnik, E. L. Signature of Planetary Mergers on Stellar Spins. ApJ **864**, 65 (2018). 1802.08260.

59. Tonry, J. L. *et al.* ATLAS: A High-cadence All-sky Survey System. PASP **130**, 064505 (2018). 1802.00879.

60. Mainzer, A. *et al.* Initial Performance of the NEOWISE Reactivation Mission. ApJ **792**, 30 (2014). 1406.6025.

61. Fitzpatrick, E. L. Correcting for the Effects of Interstellar Extinction. PASP **111**, 63–75 (1999). astro-ph/9809387.

Acknowledgements K. D.'s work was supported by NASA through the NASA Hubble Fellowship grant #HST-HF2-51477.001 awarded by the Space Telescope Science Institute, which is operated by the Association of Universities for Research in Astronomy, Inc., for NASA, under contract NAS5-26555. M.M.'s contributions were supported by the National Science Foundation under Grant No. 1909203. ACE acknowledges support by NASA through the NASA Hubble Fellowship grant #HF2-51434 awarded by the Space Telescope Science Institute, which is operated by the Association of Universities for Research in Astronomy, Inc., for NASA, under contract NAS5-26555. SRK thanks Heising-Simons Foundation for supporting his research. We thank B. Metzger, T. Matsumoto, M. Soares-Furtado and J. van Roestel for valuable discussions.

Based on observations obtained with the Samuel Oschin Telescope 48-inch and the 60-inch Telescope at the Palomar Observatory as part of the Zwicky Transient Facility project. ZTF is supported by the National Science Foundation under Grant No. AST-1440341 and AST-2034437, and a collaboration including Caltech, IPAC, the Weizmann Institute of Science, the Oskar Klein Center at Stockholm University, the University of

Maryland, the University of Washington, Deutsches Elektronen-Synchrotron and Humboldt University, Los Alamos National Laboratories, the TANGO Consortium of Taiwan, Trinity College Dublin, the University of Wisconsin at Milwaukee, IN2P3 France, Lawrence Livermore National Laboratories and Lawrence Berkeley National Laboratories. Operations are conducted by COO, IPAC, and UW. The ZTF forced-photometry service was funded under Heising-Simons Foundation grant 12540303 (PI: Graham). Some of the data presented herein were obtained at the W.M. Keck Observatory, which is operated as a scientific partnership among the California Institute of Technology, the University of California and the National Aeronautics and Space Administration. The Observatory was made possible by the generous financial support of the W.M. Keck Foundation. The Submillimeter Array is a joint project between the Smithsonian Astrophysical Observatory and the Academia Sinica Institute of Astronomy and Astrophysics and is funded by the Smithsonian Institution and the Academia Sinica. The authors wish to recognize and acknowledge the very significant cultural role and reverence that the summit of Mauna Kea has always had within the indigenous Hawaiian community. We are most fortunate to have the opportunity to conduct observations from this mountain. The National Radio Astronomy Observatory is a facility of the National Science Foundation operated under cooperative agreement by Associated Universities, Inc.

Competing Interests The authors declare that they have no competing financial interests.

Contributions K. D. identified the object, initiated follow-up observations, carried out the analysis and wrote the manuscript. M. M. and A. L. led the theoretical interpretation of the transient, created the models presented in this work and wrote the manuscript. V. K., J. E. J., A. C. E., L. A., M. M. K., R. M. L., assisted with the optical/infrared follow-up observations, data interpretation and analysis. D. C., C. C., E. K., S. R. K., R. S. and A. V. assisted with the interpretation of the data. R. D., M. J. G., F. M., M. S. M., R. L. R. and B. R. are builders of the ZTF observing system and contributed to survey operations during the observations presented here. A. M. M. assisted with analysis of NEOWISE data. N. P. and R. T. assisted with acquisition of SMA data, and carried out the SMA data analysis. L. H. Q. and L. O. S. assisted with acquistion of VLA data, and carried out the VLA data analysis. All authors contributed to the scientific interpretation.

Correspondence Correspondence and requests for materials should be addressed to K.D. (email: kde1@mit.edu).

Methods

Identification in ZTF The Zwicky Transient Facility is a wide-field optical time domain survey running out of the 48-inch Schmidt telescope (P48) at Palomar observatory[10,63]. With a field of view of 47 square degrees, the instrument achieves a median limiting magnitude of $r \approx 20.5\,\mathrm{mag}$ in 30 s exposures of the sky and a survey speed of ≈ 3750 square degrees per hour[64,65]. provide an overview of the various ZTF surveys undertaken in Phase-I of operations, and the survey scheduling system designed to carry out operations to maximize volumetric survey speed. The transient source ZTF 20aazusyv (hereafter ZTF SLRN-2020) was first detected in the ZTF difference imaging pipeline on UT 2020-05-16 (MJD 58985.37) at J2000 coordinates α =19:09:39.78 and δ =+05:35:04.25, and at a magnitude of $r = 20.03 \pm 0.19\,$mag. The corresponding Galactic coordinates are $l = 39.979890$, $b = -1.48927$, placing this source in the direction of Galactic disk. The transient was not detected on MJD 58983.38 to a 5σ limiting magnitude of $r = 20.48$. We nominally adopt the mid-point of the last non-detection and the first detection of the transient in r-band (MJD 58984.38) as the time of start for the eruption.

We identified ZTF SLRN-2020 as a candidate classical nova as part of an ongoing systematic search for Galactic novae in optical/near-infrared (NIR) time domain surveys[66]. Nova candidates were identified in the public ZTF alert stream (g and r filters) by selecting for slow-evolving, large amplitude Galactic plane transients through a custom filter implemented on the `kowalski` time domain astronomy server[67]. The selection criteria were as follows:

1. The transient should be located within 10 degrees of the Galactic plane.

2. The transient should have no prior history of outbursts in the ZTF alert archive.

3. The transient should have brightened by > 3 mag from the nearest counterpart in the PanSTARRS1 (PS1) source catalog[68], if one exists within 2 arcsec; or the source should have no known PS1 counterpart within 2 arcsec.

4. The transient should exhibit a slow evolving light curve with $t_2 > 30$ days, where t_2 is the time taken to fade by 2 magnitudes from the peak of the outburst. This criteria distinguishes classical novae from the majority of dwarf nova outbursts that exhibit fast evolving light curves with $t_2 < 30$ days[11].

Photometry from ground-based time domain surveys We retrieved gri photometry of the transient from data taken with the P48 ZTF camera[10], that were processed with the ZTF data processing system[70]. Light curves were extracted using forced point spread function (PSF) photometry[70] at the location of the transient in the difference images[71], where the location was determined from the median of the positions in all published alerts of the transient. We report detections in the forced photometry for epochs where the signal-to-noise ratio (SNR) is higher than 3σ, while 5σ upper limits are reported for other epochs. While the g and r-band data were acquired as part of the ongoing ZTF public survey, the i-band data was acquired as part of an internal collaboration survey where the reference images were contaminated by the transient emission and therefore non-trivial to remove. We thus chose to use i-band photometry reported as part of the PSF-fit source catalogs[70] for each observation, where the transient is detected starting from the first i-band observation of the field on UT 2020-04-16 until the end of the observing season. As the transient was brightest in

i-band, we use the peak of the i-band light curve as the reference phase for all other observations.

Given the high cadence of the ZTF data as well as the relatively slow evolution of the transient, we performed an inverse variance weighted binning of the flux measurements in bins of 3 days to improve the SNR and report them in Table 1; however, we also show the 1-day cadence early time ZTF i-band light curve in Figure 1. We perform the same binning for reporting upper limits, where we use inverse variance weighted flux uncertainty to report the 5σ upper limit for each epoch. We also retrieved forced photometry at the source location from data taken with the Asteroid Terrestrial-impact Last Alert System (ATLAS) survey[59] using the public photometry service[1]. We performed binning using the same method on the ATLAS data and the transient emission is clearly detected in both the c and o filters. The ZTF and ATLAS photometry are presented in Table 1 and shown in Figure 1.

Mid-IR NEOWISE Photometry The transient location was observed during the ongoing NEOWISE all-sky mid-IR survey in the $W1$ ($3.4\,\mu$m) and $W2$ ($4.6\,\mu$m) bands[60,73]. We retrieved time-resolved coadded images of the field created as part of the unWISE project[75,76]. Due to the location of the source in a crowded field with nearby blended sources (Figure 1), we used a custom code[77] based on the ZOGY algorithm[71] to perform image subtraction on the NEOWISE images using the full-depth coadds of the WISE and NEOWISE mission (obtained during 2010-2014) as reference images. Photometric measurements were obtained by performing forced PSF photometry at the transient position on the subtracted NEOWISE images until the epoch of the last NEOWISE data release (data acquired until December 2021). Transient mid-IR emission is clearly detected in the

[1] https://fallingstar-data.com/forcedphot/

subtracted images starting ≈ 250 days prior to the optical outburst peak. The template-subtracted NEOWISE photometry are provided in Table 2 and shown in Figure 1.

Swift Observations We obtained X-ray follow-up of the transient with the Swift X-ray telescope (XRT[78]) on the Neil Gehrels Swift Observatory (Swift[12]). The Swift observatory observed the location of the transient on UT 2020-11-04 ($\approx$ 160 days after i-band peak) for a total exposure time of 1.35 ks. No source was detected at the location of the transient down to a 3σ limiting flux of 8.3×10^{-3} count s^{-1}, corresponding to a 0.3–10 keV flux of 2.8×10^{-13} ergs cm^{-2} s^{-1} for a photon index of $\Gamma = 2$. In the same observation, no source was detected with the Ultraviolet Optical telescope (UVOT[80]) in the UVW2 filter, down to a 3σ limit of 22.69 AB mag. The X-ray non-detection constrains the X-ray luminosity of the source to be $\lesssim 5.3 \times 10^{32} (d/4\,\mathrm{kpc})^2$ erg s^{-1} at this phase, and therefore is much fainter (even if placed at ≈ 20 kpc) than accretion events around neutron stars or black holes that reach at least $\gtrsim 10^{35}$ erg s^{-1} during the outburst[13, 82].

NIR imaging follow-up We obtained NIR imaging of the transient location on UT 2021-03-31 and UT 2022-07-23 with the Wide-Field Infrared Camera (WIRC[83]) on the Palomar 200-inch telescope. We obtained dithered exposures of the field for a total exposure time of 495 s, 330 s and 330 s respectively in the J, H and Ks filters respectively on each epoch. The data were reduced using standard techniques including dark subtraction, flat-fielding, sky subtraction, astrometric and photometric calibration[66]. For the image taken in 2021 March when the transient was bright (Figure 1), we performed aperture photometry on the reduced images at the position of the transient[2]. The resulting magnitudes are $J = 16.64 \pm 0.02$, $H = 15.42 \pm 0.02$ and $Ks = 14.67 \pm 0.01$ on UT

[2]We provide all IR magnitudes in the Vega system.

2021-03-31.

Given the crowded nature of the field as well as marginal evidence for blended sources near the transient location in the WIRC images, we obtained additional high spatial resolution Adaptive Optics (AO) assisted imaging using the Gemini South Adaptive Optics Imager (GSAOI) on the Gemini-S telescope[84,85]. The source was observed on UT 2022-04-15 as part of a Director's Discretionary Program (GS-2022A-DD-102; PI: K. De). We obtained dithered exposures of the field using Laser Guide Star (LGS) correction for a total exposure time of 300 s on source and 300 s off the source (for background subtraction) in J-band[3]. The raw images were detrended and stacked using the `DRAGONS` pipeline[86], using the source catalog from the WIRC images for astrometric and photometric calibration. The transient is clearly detected in the GSAOI images together with an unrelated nearby point source $\approx 0.6''$away (Figure 1).

We use the GSAOI images to measure the best position of the transient source to be at J2000 coordinates α =19:09:39.783 and δ = +05:35:04.269. The coordinates of the unrelated nearby source are α = 19:09:39.815 and δ = +05:35:04.064. The typical positional uncertainty is estimated to be $< 0.05''$by cross-matching against the Gaia DR3 catalog. We perform aperture photometry at the location of the transient to obtain a flux of $J = 19.17 \pm 0.05$ mag. We use the GSAOI positions to derive flux measurements for the transient source detected in the multi-band WIRC images from 2022 July. The source is clearly blended with the unrelated nearby source in the WIRC images, and we fit the image around the position of the transient with a `tractor`

[3]Observations were also obtained in the H and K filters with GSAOI but were unusable due to poor atmospheric conditions.

model[87] to obtain deblended flux measurements. We fix the position of the transient and nearby source as measured from the GSAOI images, and jointly fit the flux of the two sources using the measured PSF of the image to minimize the residual χ^2 using the Markov Chain Monte Carlo library `emcee`[88]. The resulting flux measurements for the transient are $J = 19.17 \pm 0.15\,$mag, $H = 17.75 \pm 0.09\,$mag and $Ks = 17.13 \pm 0.10\,$mag.

Archival optical/IR observations The location of the transient was covered prior to the outburst in the United Kingdom Infrared Telescope (UKIRT) Galactic plane survey[26] between 2007 and 2011. A faint progenitor is detected at the position of the transient as well as reported in the UKIRT source catalog. However, the source is clearly blended with the unrelated nearby source detected in the GSAOI images, and the photometric measurements are contaminated with the nearby source as confirmed by the shifted position of the flux centroid with respect to the transient position in the GSAOI images. In order to obtain improved flux measurements for the progenitor counterpart, we fit a `tractor` model[87] to the UKIRT image as in the case of the late-time WIRC images. The source is detected in the H and K bands, but fainter than the 3σ detection threshold in J-band; we tabulate the measured fluxes from the `tractor` modeling in Table 3. The source location was also covered in optical images acquired in the PanSTARRS1 survey[68], but the progenitor was not detected. We obtained 5σ upper limits on the progenitor optical flux by querying the PS1 source catalog in a $2'$ region around the position and estimating the median magnitude of sources at the 5σ detection threshold. The flux limits are reported in Table 3.

Spectroscopic follow-up Following the identification of the transient, we obtained one epoch of optical spectroscopy and one epoch of near-infrared spectroscopy of the outburst using the

Low Resolution Imaging Spectrometer (LRIS[90]) on the Keck-I telescope and TripleSpec[91] on the Palomar 200-inch telescope respectively. The LRIS data were reduced using standard techniques using an automated pipeline[92], while the TripleSpec data were reduced using the `spextool` pipeline[93] followed by telluric correction and flux calibration using `xtellcor`[94]. The spectra obtained during the outburst are summarized in Table 4. We obtained two epochs of near-infrared spectroscopic follow-up of the infrared remnant star ≈ 2 years after the outburst using the Folded-port Infrared Echellette (FIRE[95]) on the Magellan Baade telescope and one epoch using the Near-Infrared Echellette Spectrometer (NIRES[96]) on the Keck-II telescope. The observing setups are summarized in Table 4. The FIRE data were reduced using the `pypeit` code[97] for the echelle mode data and the `firehose` pipeline[98] for the prism mode data. The NIRES data were reduced as the TripleSpec data using the `spextool` pipeline[93], followed by telluric correction using the `xtellcor` pipeline[94]. As the late-time data were acquired close in time (Table 4), we performed an inverse variance weighted stacking of the spectra to improve the signal-to-noise ratio. The individual spectra were flux calibrated to match the contemporaneous late-time JHK photometry obtained from WIRC, and the stacked spectrum was binned to the resolution of the Keck-NIRES data ($R \approx 2700$). The final reduced and stacked spectra are shown in Figure 3.

VLA SiO maser search Two hours of Director's Discretionary Time was awarded on NSF's Karl G. Jansky Very Large Array (VLA) to observe the field of ZTF SLRN-2020 at 43 GHz using the most extended (A-array) configuration on 2022 April 14 under project 22A-464 (PI: De). The observations, of which about 53 minutes on ZTF SLRN-2020, were set up to be sensitive to any SiO (maser) emission between 42.25 and 43.5 GHz. The SiO transitions were targeted to possibly help confirm the peculiar giant merger product and to possibly measure its line-of-sight velocity to get a constraint on a (kinematic) distance to support its remarkable low luminosity.

The observations used 3C286 to calibrate the flux density scale and the instrumental bandpass response. Antenna pointing calibration in the direction of the target field was performed using J1851+0035, whereas the gain and reference calibrator J1912+0518 observed 50 cycles of 25 seconds while interspersing the 65 second observations of ZTF SLRN-2020 using a cycle time of 2 minutes (with a slew time of about 10 seconds each way). The data were inspected for bad visibilities and further processed using the general PIPEAIPS pipeline reduction procedure in AIPS. Calibration and imaging did not reveal any potential issues and the resulting synthesized beam measured about 65 by 45 mas at a position angle of -60 degrees. The calibrator J1912+0518 was measured to have a flux density of about 88 ± 2 mJy/beam.

The setup was in particular targeting the (J=0-1) v=1 and v=2 transitions using a channel width of 62.5 kHz (≈ 0.5 km/s) to an RMS level of ≈ 6 mJy/channel, although all seven possibly detectable transitions were covered using 1 MHz (≈ 7 km/s) channels with an RMS of ≈ 1.2 mJy/channel. The $\sim$1.2 GHz line-free continuum bandwidth at 43 GHz was imaged down to an RMS of $\approx 35\mu$Jy/beam. No significant SiO line nor continuum emission was detected in the several arcseconds surrounding the infrared position of ZTF SLRN-2020, down to the 3.0σ flux uncertainty within 0.2" of the expected position. For the line emission, we searched up to ≈ 60 MHz (± 420 km/s) of the transition rest frequencies which is a conservative upper limit for objects bound to the Galaxy.

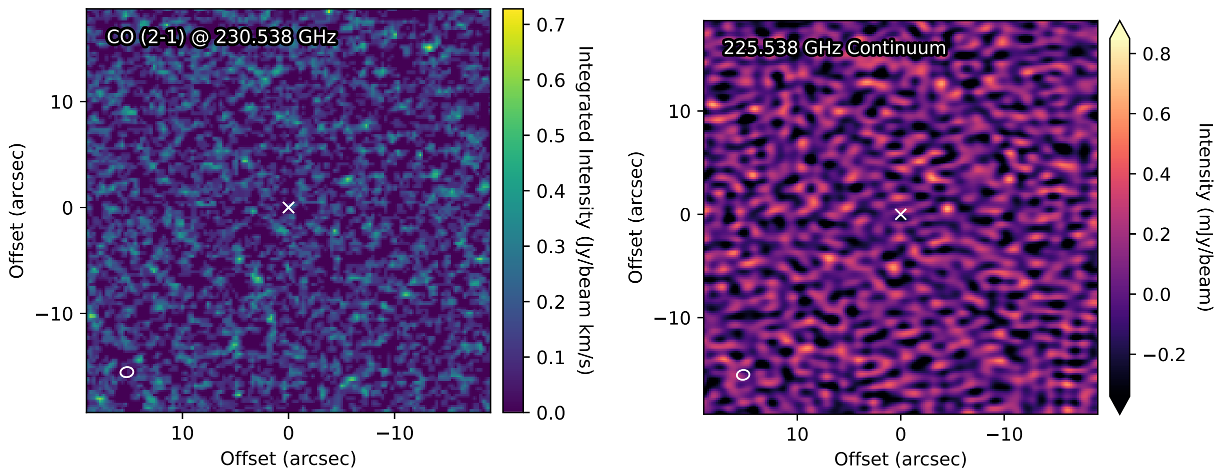

Figure 5: Integrated CO line intensity map (2-1 transition at 230.538 GHz; left) and continuum intensity map (at 225.538 GHz; right) from Submillimeter Array observations centered at the position ZTF SLRN-2020 (shown with a white cross). The white ovals in the lower left corner of the images show the shape of the synthesized beam ($1.2'' \times 0.9''$; PA = $-82°$) from the observations.

SMA search for sub-mm molecular emission

ZTF SLRN-2020 was observed with the Submillimeter Array on two epochs: 15 March 2022 and 17 June 2022. The CO 2-1 line and continuum emission maps after combining the data from both the epochs, are shown in Figure 5. The SMA was in the extended configuration in both the epochs, with 6 antennas operating in the array. The phase center coordinates were RA(2000) = 19:09:38.78, DEC(2000) = +05:35:04.3. Both the 230 and 240 GHz receivers were tuned to place the frequency of the CO 2-1 line, 230.538 GHz, in the spectral window 1 in the upper sideband (with each sideband providing 12 GHz of frequency coverage). With this tuning, the lower sideband covered 209.5 to 221.5 GHz and upper sideband: 229.5 to 241.5 GHz. The spectral resolution is 140 kHz, but the raw data were smoothed to an effective resolution of 1 MHz per channel. The primary gain calibrator was 1830+063, observed periodically for 4 min, following the integration for 15 minutes on the target source. The quasars 3C279 and BL Lac were observed for 2 hours each, to provide bandpass calibration. Absolute fluxes were calibrated using observations of MWC349a, Mars and Callisto. In the first epoch, the system temperature varied from 80 to 200K, with the atmospheric zenith optical depth (at 225 GHz) ≈ 0.1. The weather was better in the second epoch, with $\tau_{225} = 0.06 - 0.08$, and system temperatures varying from $80 - 150\,$K.

The SMA data were reduced using the Millimeter Interferometer Reduction (MIR) software using the online procedure[4]. The resulting calibrated visibility data were imaged using the Common Astronomy Software Application (CASA)'s tclean task. We imaged a range of channels covering a velocity interval of about 100 km/s around the CO 2-1 line, producing a data cube of channel maps. The synthesized beam size in the combined observations was $1.25 \times 0.85''$, with PA of 104.2°. No source is detected at the postion of the transient. The combined (including both datasets) continuum sensitivity is 0.17 mJy/beam while for an individual channel for the CO cube is 14.3 mJy/beam over 3 km/s.

Photometric analysis We compare the high cadence r and i-band light curves of ZTF SLRN-2020 to a sample of known red novae from the literature in Figure 6. ZTF SLRN-2020 broadly exhibits a fast rise to peak starting ≈ 10 days prior to outburst peak followed by a slow decay of ≈ 2.5 mag over ≈ 200 days. While the Galactic objects V1309 Sco and OGLE-BLG-360 exhibit a long and slow rise prior to the peak of the light curve, the photometric behavior of ZTF SLRN-2020 around peak is similar to V838 Mon. The fast rise and slow decay of ZTF SLRN-2020 is also similar to many extragalactic red novae (e.g. AT 2018hso and AT 2017jfs) but the duration is longer than

[4] `https://lweb.cfa.harvard.edu/rtdc/SMAdata/process/mir/swarm_example/`

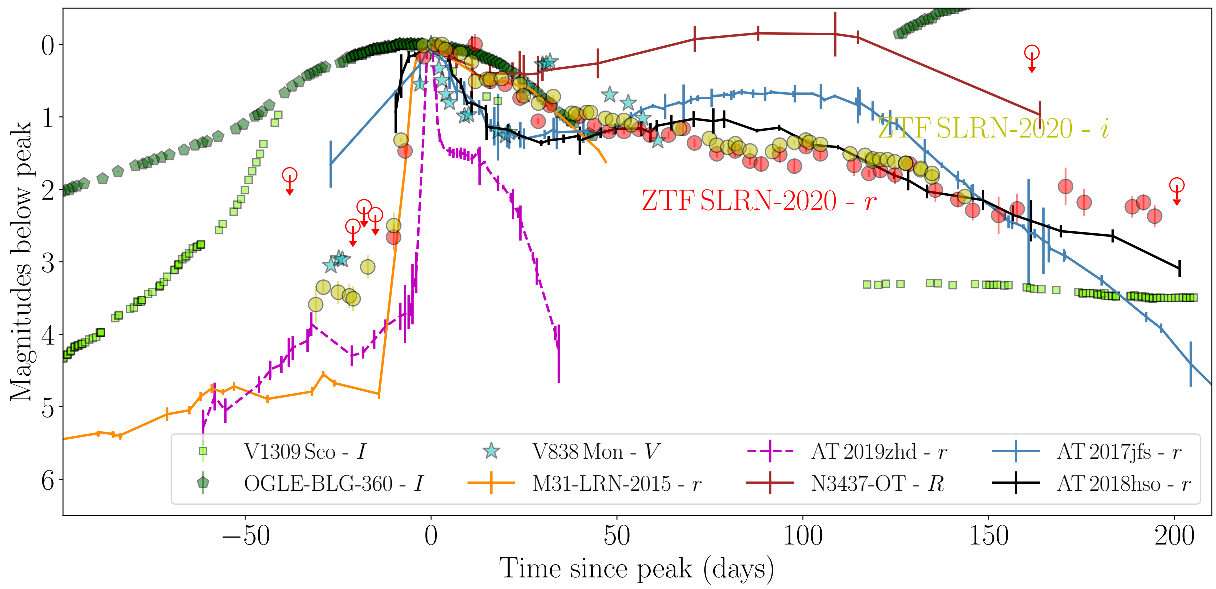

Figure 6: Comparison of the r and i band light curve of ZTF SLRN-2020 (shown as red and yellow circles respectively, as indicated) to visual light curves of Galactic and extragalactic red novae from the literature. The light curves have been normalized to peak magnitude. For each comparison object, we indicate the photometric band of the archival light curve in the legend. The comparison objects include V1309 Sco[9], OGLE-BLG-360[21], V838 Mon[101], M31-LRN-2015[31,103], AT 2019zhd[104], NGC 3437-OT[105], AT 2017jfs[106] and AT 2018hso[107].

the fast decay of AT 2019zhd after peak. ZTF SLRN-2020 also exhibits a rapid decay around $\approx$ 30 days after light curve peak, similar to AT 2019zhd but with a smaller drop in magnitude. Additionally, the pre-outburst i-band variability of ZTF SLRN-2020 is similar to that of V838 Mon as well as the nearby red novae in M31 (M31-LRN-2015 and AT 2019zhd) where the progenitor variability was detected prior to the main outburst.

In Figure 7, we also compare the color evolution of ZTF SLRN-2020 to objects in the literature. ZTF SLRN-2020 exhibits a rapid reddening around the peak of the outburst followed by a slow reddening of the $g - r$ color, while the $r - i$ color remains relatively constant. Similar reddening of the $g - r$ color is also seen in the literature red novae, although the magnitude of

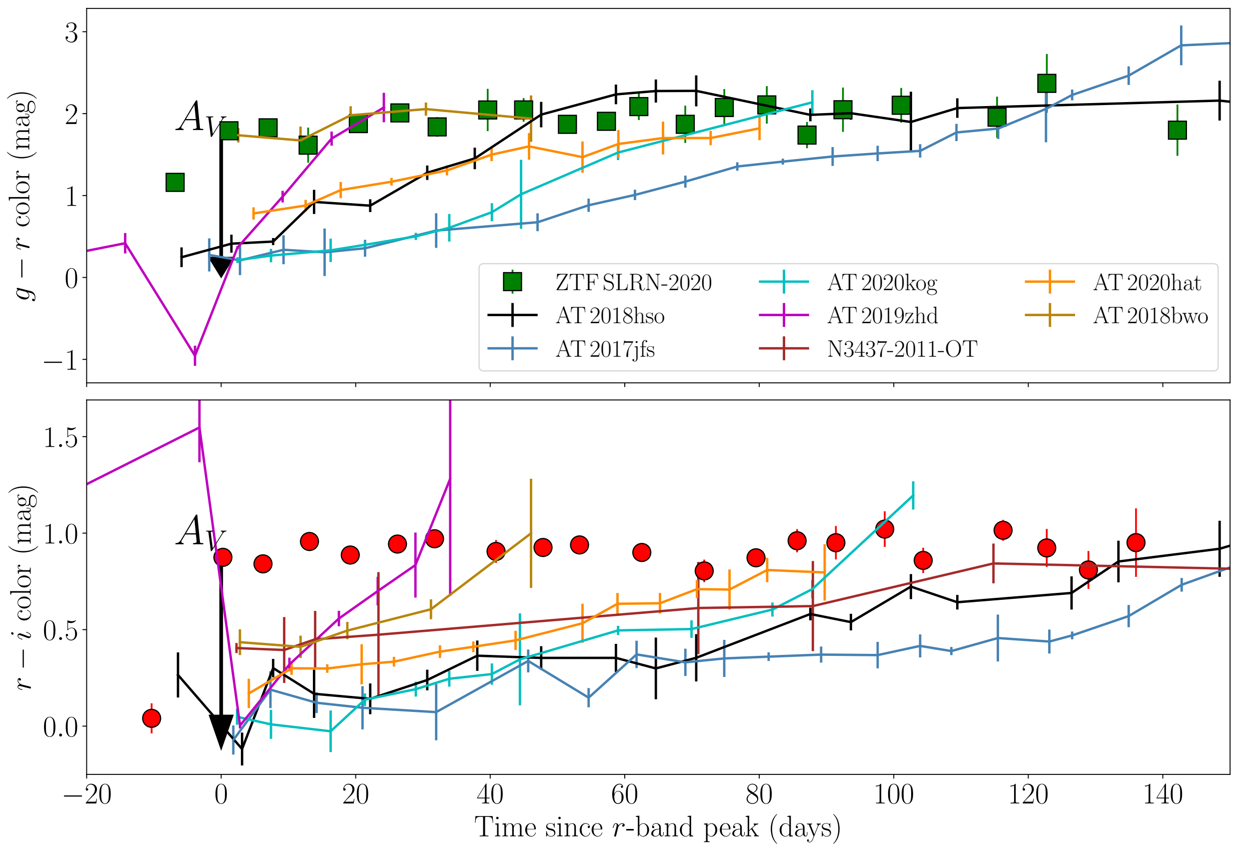

Figure 7: Comparison of the $g - r$ (top panel) and $r - i$ (bottom panel) observed color evolution of ZTF SLRN-2020 (shown as squares and circles respectively) to a sample of red novae from the literature that have contemporaneous multi-band coverage during the outburst. The literature objects include some of the objects shown in Figure 6 in addition to AT 2020hat, AT 2020kog[108] and AT 2018bwo[109]. In each panel, we show a black arrow indicating the estimated shift in the color evolution of ZTF SLRN-2020 accounting for the best estimated line-of-sight extinction.

the progressive reddening is larger for these objects during the ≈ 100 days after peak. The slow $g - r$ color evolution of ZTF SLRN-2020 is most similar to AT 2018bwo, which also exhibits only a small change in the color over the first ≈ 40 days, while the slow $r - i$ color evolution is most similar to AT 2017jfs. Accounting for the estimated foreground Galactic extinction (see Spectral Energy Distribution Evolution), ZTF SLRN-2020 remains relatively blue compared to the literature sample. As the progressive reddening with time is attributed to the cooling of an expanding photosphere in red novae followed by dust formation[109], the relatively slow evolution in ZTF SLRN-2020 may be related to a lower amount of photospheric expansion and dust formation relative to other objects, consistent with the modeling of the bolometric light curve and SED (see Spectral Energy Distribution Evolution).

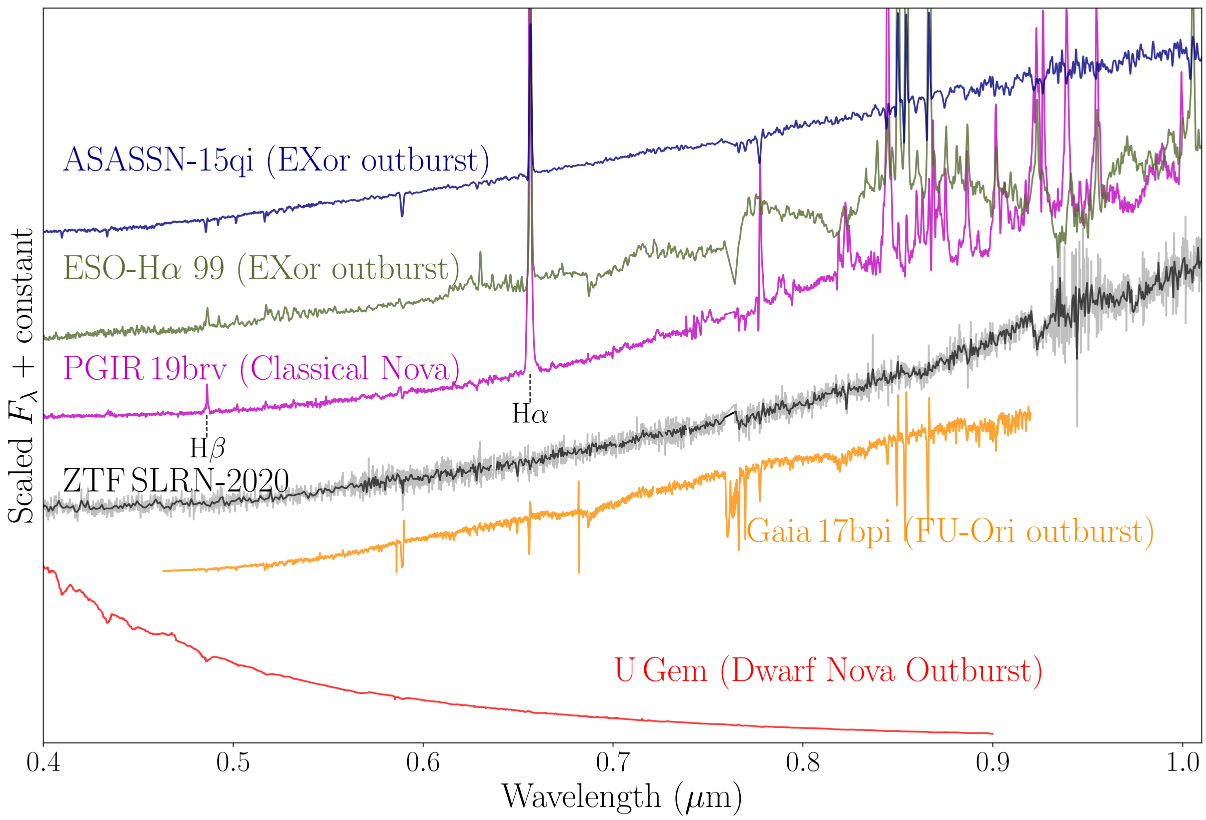

Figure 8: Comparison of the optical spectrum of ZTF SLRN-2020 to different types of Galactic transients, including a classical nova (PGIR 19brv[66], in magenta), a dwarf nova (U Gem[110] in red) and a FU-Ori type young star outburst (Gaia 17bi[111] in yellow) and two EXor type young star outbursts (ESO-Hα 99[112] in green and ASASSN 15qi[113] in blue). The continua of some sources have been reddened to match that of ZTF SLRN-2020 for easier visualization.

Spectroscopic features The optical outburst spectrum of ZTF SLRN-2020 (Figure 3) exhibits a relatively featureless continuum with only atomic/molecular absorption features of Na, Ba II, Hα, Mg II, TiO and VO. The TiO molecular bands are characteristic in the spectra of cold, late-type giant stars, with later type giants exhibiting deeper absorption features[114,115]. To identify the corresponding spectral type, we compared the spectrum of ZTF SLRN-2020 to a library of stellar spectra from the VLT X-shooter spectral library[116], and found a good match of the TiO/VO line depths to the M4-III type giant HV 2255. We applied a foreground extinction of $A_V = 5.5\,\mathrm{mag}$[5] to the spectrum of the comparison star using a standard Fitzpatrick extinction law[61] and show the comparison in Figure 3. The inferred spectral type corresponds to an effective photospheric temperature of $\approx 3600\,\mathrm{K}$[118].

The optical spectrum shows a strong absorption line in the Na D doublet. We measure the total equivalent width (EW) of the line by fitting a polynomial to the absorption feature, and measure the uncertainty by creating 1000 realizations of the spectrum by adding Gaussian noise scaled to the root-mean-square noise in the adjacent part of the spectrum. We find $EW = 3.65 \pm 0.75\,$Å. The strength and profile of the Na D line is known to vary with time in many types of explosive transients[119,120], and has recently been shown to be time-varying in extragalactic red novae[121]. The line becomes stronger with time in red novae, likely due to the condensation of dust in the envelope. As a result, we are unable to use the Na D feature as an indicator of the foreground extinction as for other types of Galactic transients[66,122].

The spectra of ZTF SLRN-2020 show no signatures of emission lines indicative of hot gas in the eruption, as commonly seen in other types of Galactic plane transients. In Figure 8, we compare the optical spectrum of ZTF SLRN-2020 to other common types of Galactic stellar outbursts.

[5]The A_V used here is consistent with the inferred total dust optical depth modeled in the Spectral Energy Distribution Evolution.

While classical novae exhibit strong and broad emission lines of the Balmer series and nuclear processed material[17], accretion outbursts in binary white dwarf systems (i.e. the dwarf novae) exhibit strong Balmer absorption features together with Hα in emission, indicative of the hot gas in the accretion process. Similarly, the outbursts of young stars exhibit strong emission lines at all phases indicative of hot gas in the outflowing material. Unlike the years-to-decades long outbursts of the FU Ori stars[15], the light curve of ZTF SLRN-2020 is similar to that of the EXor class of young stars that exhibit few month long outbursts[125]. However, the optical spectra of EXor outbursts are dominated by a forest of emission lines of atomic species like H and Ca II at all phases[126], indicative of magnetospheric disk emission[127], unlike that seen in the optical spectra of ZTF SLRN-2020 (Figure 8). While red novae also exhibit emission lines at early phases[103,109,121,128], the lines become progressively weaker with time as the photosphere becomes dominated by molecular absorption features from the newly formed molecules and dust[105], similar to that seen in the spectrum of ZTF SLRN-2020 around 6 months after outburst peak (Figure 3).

Figure 3 shows NIR spectra of ZTF SLRN-2020 obtained during the outburst ($\approx$ 160 days after peak) and after the fading of the infrared transient ($\approx$ 690 days after peak). We show a zoom-in of the spectra of the individual bands in Figure 9. We identify broad molecular absorption features of H_2O affecting the continua of the H and K-bands. In addition, we identify bandheads of TiO and VO in J-band together with weak ^{12}CO absorption bandheads in K-band. The lack of strong emission lines of hydrogen (e.g. in the Paschen and Brackett series) as well as the CO band-heads which are ubiquitous in EXor type outbursts[125,126] further distinguishes ZTF SLRN-2020 from the population of young star outbursts.

Comparing the spectra to stars in the IRTF Spectral Library[129], the broad H_2O absorption bands and weak molecular absorption features are reasonably matched to a M7-III type star, and we show the comparisons in Figures 3 and 9. We note that although the NIR spectrum was obtained near the optical spectrum, the NIR spectrum suggests a later spectral type than the optical spectrum. Such differences have also been identified in the late-time spectra of previous Galactic red novae[24,130], where the extremely low gravity in the extended envelope of the remnant enables the formation of H_2O molecules and pushes the condensation of TiO and VO to low temperatures. The very late-time spectrum of ZTF SLRN-2020 does not show distinctive absorption features seen during the outburst, except for the broad H_2O absorption bands in H and K-band. Unlike the NIR spectrum in outburst, the late-time spectrum exhibits a clear rising continuum towards redder wavelengths in K-band, indicative of warm dust emission as inferred from the modeling of the spectral energy distribution.

Spectral Energy Distribution Evolution The outburst of ZTF SLRN-2020 was detected in multiple time domain surveys with wavelength coverage extending from the optical g-band to mid-IR WISE-$W2$ band. While the optical emission likely arises from a hot photosphere, the bright mid-IR emission is indicative of a warm dust shell around the eruption. Here, we model the optical to mid-IR SED of the transient to estimate the time evolving properties of the optical photosphere and dust shell. We use the radiative dust transfer code `DUSTY`[132,133] to fit the multi-wavelength data. We assume a spherically symmetric distribution of the dust with a $\propto r^{-2}$ density profile around the star, which is assumed to be a point source. We assume the dust grains to be composed of warm silicates as indicated by the O-rich composition of the photospheric spectra[134], and with a MRN

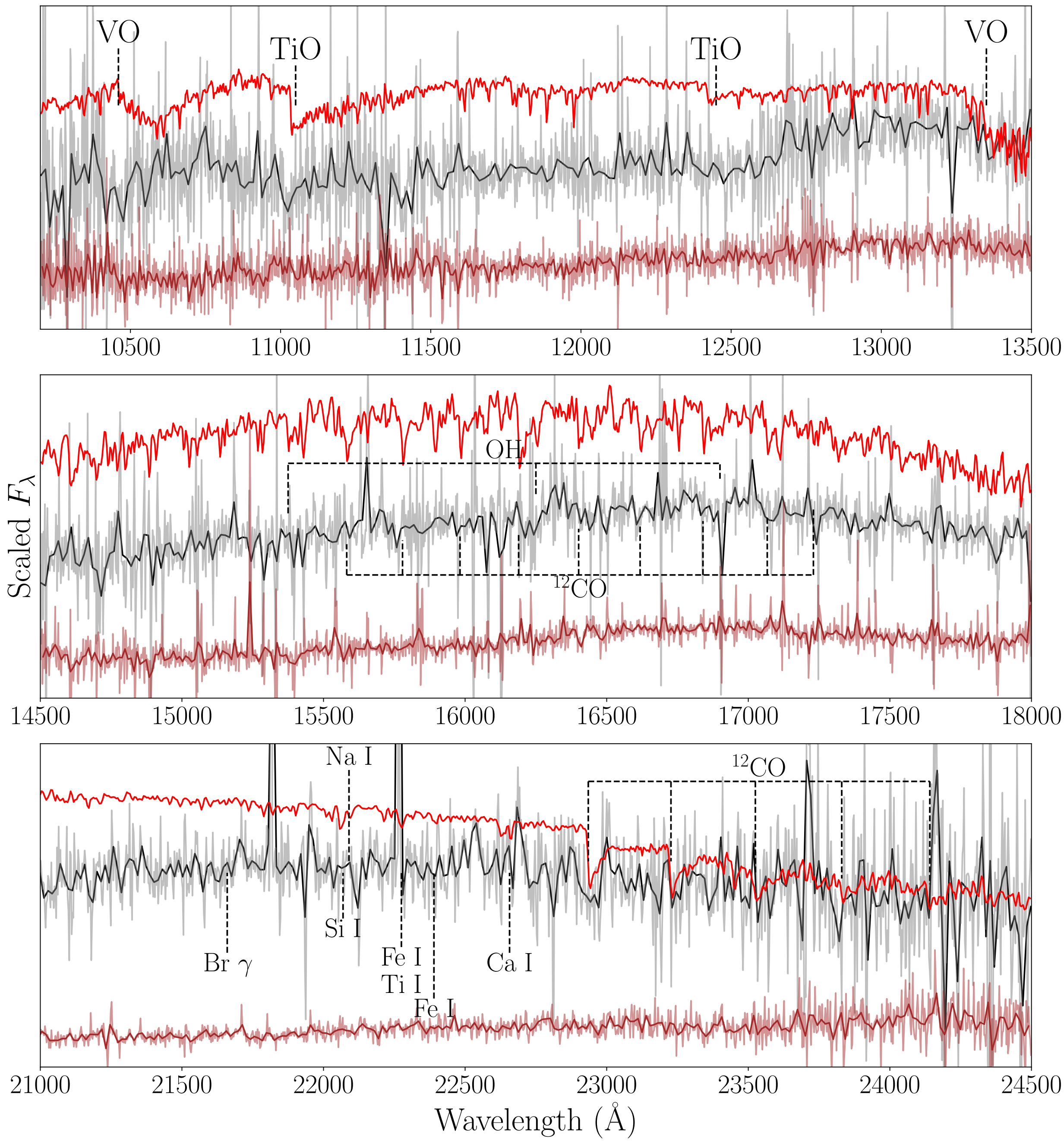

Figure 9: Identification of spectroscopic features in the NIR spectra of ZTF SLRN-2020 during and after the outburst. In each panel, the gray/black lines represent the raw/binned spectrum during the outburst ($\approx$ 160 d after peak), while the light brown/brown lines show the raw/binned spectrum obtained after the fading of the infrared transient ($\approx$ 690 d after peak). We also show a comparison with the M7-III type star HD 108849 (in red). Prominent atomic and molecular absorption features are marked.

grain size distribution[135] ($\propto a^{-3.5}$) with a minimum and maximum grain size of $a_{min} = 0.005\,\mu$m and $a_{max} = 0.25\,\mu$m. We fix the thickness of the dust shell to be $Y = 5\times$ the inner radius (r_{in}) of the shell; the model SEDs are found to be relatively insensitive to this assumption since the $3 - 5\,\mu$m emission arises primarily from the hotter, inner part of the dust shell.

We fit the observed SED of ZTF SLRN-2020 at two epochs during the outburst that have NEOWISE mid-IR coverage (≈ 120 and ≈ 320 days after outburst peak; shown in Figure 1) using a Markov Chain Monte Carlo (MCMC) wrapper around the `DUSTY` code[136] using the Python `emcee` library[88]. We model the foreground wavelength-dependent interstellar extinction using a Fitzpatrick law[61] extending from the optical to the mid-IR. The resulting free parameters of the model are the dust optical depth at $0.55\,\mu$m (τ_V), the foreground visual extinction (A_V), the inner stellar temperature (T_*), the dust temperature at the inner edge of the shell (T_d) and the total flux (F). We assume flat priors on all the fit parameters and ensure convergence of the posterior sampling chains. As multi-color optical detections were available only at the ≈ 120 d epoch, we keep A_V as a free model parameter for this epoch, but fix it at the best derived value from the 120 d epoch when fitting the 320 d epoch. Nevertheless, we find that the best fit for the 320 d epoch is relatively insensitive to the assumed A_V since all the photometric data at this epoch are in the infrared bands, where the foreground extinction is less important (e.g. $A_K \approx 0.3 - 0.4$ mag).

The best-fit parameters were derived using the median of the posterior sample distribution while their confidence intervals are derived from the 16th-84th percentile (68% confidence) interval of the distributions. The derived parameters and their uncertainties are listed in Table 5, and shown in Figures 10 and 11. During the outburst (≈ 120 d after peak), the SED is well described by an

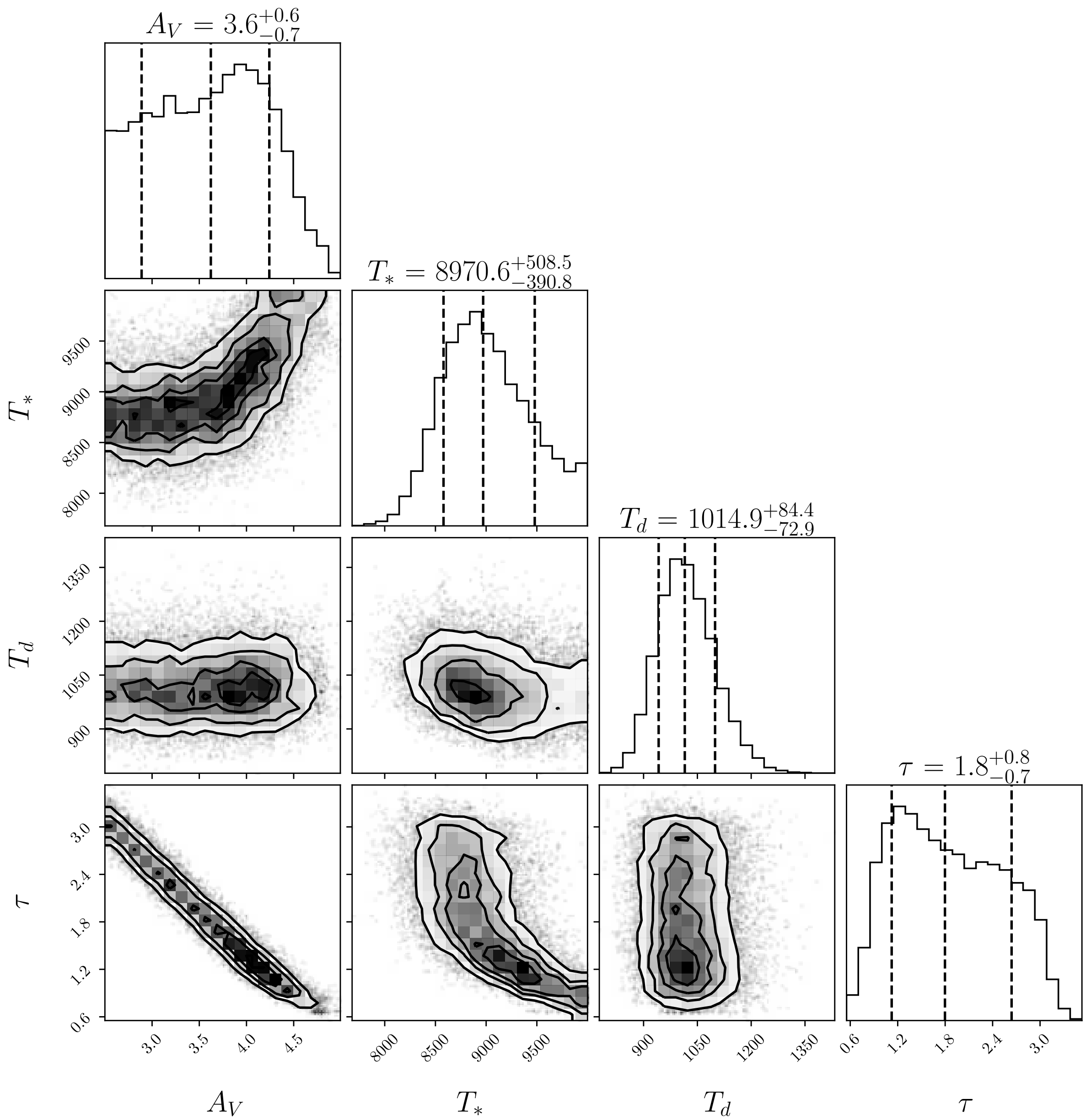

Figure 10: Corner plots showing the model-fit parameters of the MCMC `DUSTY` modeling of the SED of ZTF SLRN-2020 ≈ 120 days after outburst peak.

inner photosphere with a temperature of ≈ 8900 K surrounded by a warm dust shell with $T_d \approx$ 1020K. The optical depth of the dust ($\tau_V \approx 1.8$) is relatively low at this epoch. The foreground extinction is $A_V \approx 3.6$ mag, although this parameter is degenerate with the optical depth of the

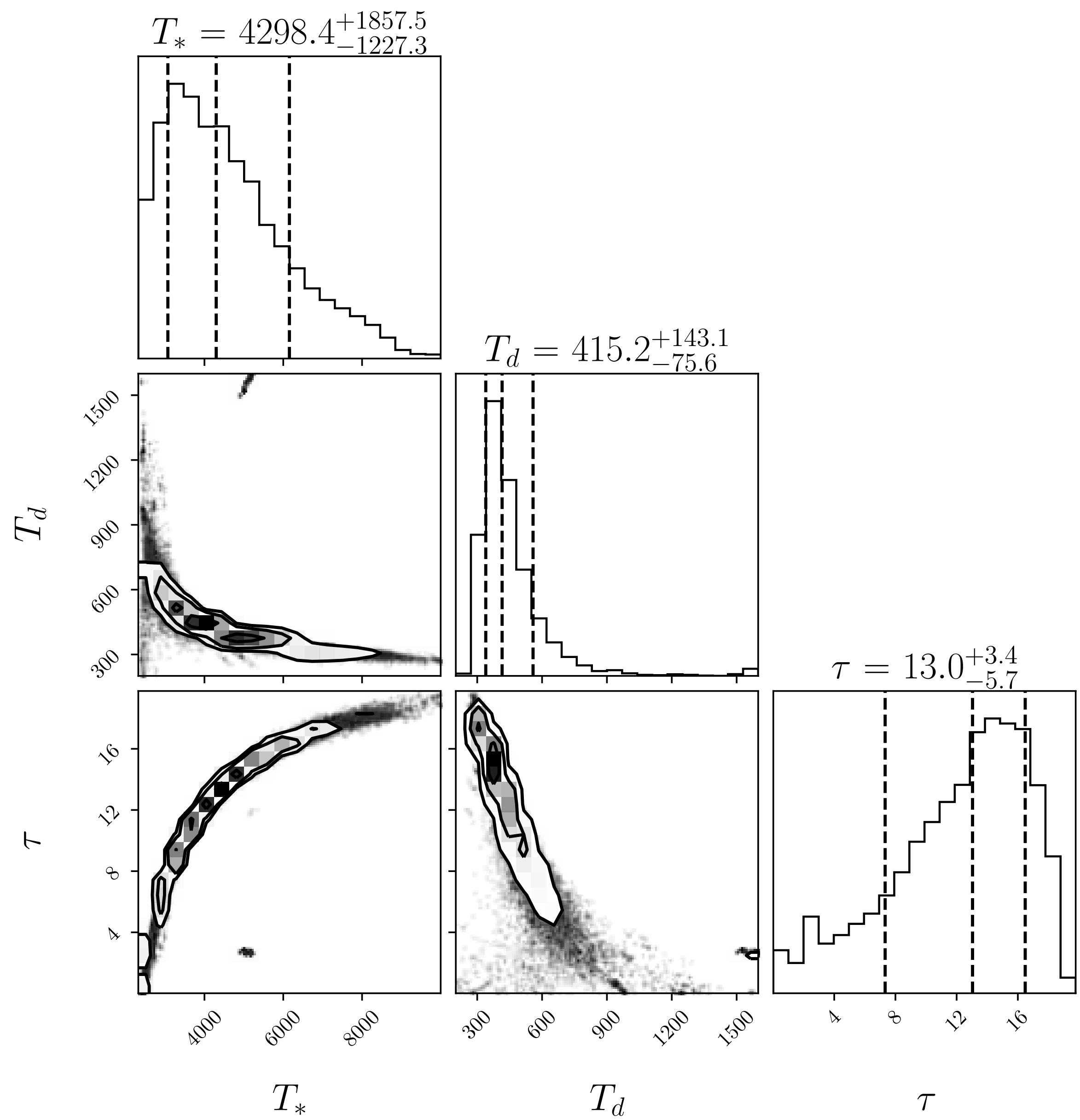

Figure 11: Corner plots showing the fit parameters of the MCMC DUSTY modeling of the SED of ZTF SLRN-2020 ≈ 320 days after outburst peak (A_V is not used as a free parameter in this fit).

dust shell. While multi-epoch mid-IR data is scarce for the literature sample of red novae, similar parameters involving a relatively hot photosphere surrounded by a low optical depth dust shell were also derived at similar phases in DUSTY modeling for the nearby red nova M31-LRN-2015[103].

Towards the end of the outburst ($\approx 320\,$d after peak), the DUSTY fitting suggests that both the internal photosphere and the surrounding dust shell have cooled substantially, while the optical depth of the dust has increased by a factor of ≈ 6.

We estimate the total mass of the dust shell at an epoch[103] as,

$$\frac{M_d}{M_\odot} \approx 3.06 \times 10^{-7} \left(\frac{100\,\mathrm{cm}^2\,\mathrm{g}^{-1}}{\kappa_V}\right) \left(\frac{r_{in}}{1000\,R_\odot}\right)^2 \tau_V \tag{1}$$

where M_d is the dust mass and $\kappa_V \approx 50 - 100\,\mathrm{cm}^2\,\mathrm{g}^{-1}$ is the dust opacity for a typical dust-to-gas ratio[134]. In order to derive r_{in}, we assume a distance of $4\,$kpc, as indicated by the distance estimates derived in the Spectral Energy Distribution evolution, and list the corresponding radius and mass values in Table 5. The observed increase in the dust shell inner radius between the ≈ 120 and $\approx 320\,$days epochs suggests an expansion velocity of $v_{ej} \approx 35\,\mathrm{km\,s}^{-1}$. The low inferred velocity of the shell suggests that signatures of such an outflow would be difficult to detect in our low resolution spectra. Together with the increase in the optical depth, the increased dust mass suggests that dust formation in the ejecta shifts the SED of the transient from the optical to the IR bands. Similar abrupt dust formation has also been observed in previous red novae[9,25,103]. The mass estimate provides a lower limit to the total (dust + gas) ejecta mass of $\approx 10^{-6}\,\mathrm{M}_\odot$, noting that only a fraction of the ejecta has likely reached the dust condensation radius within a year after the outburst[103,138].

Distance constraints and bolometric light curve We use the inferred foreground dust extinction to ZTF SLRN-2020 to place constraints on the distance to the source. In Figure 12, we show published three dimensional Galactic dust extinction maps at the location of ZTF SLRN-2020

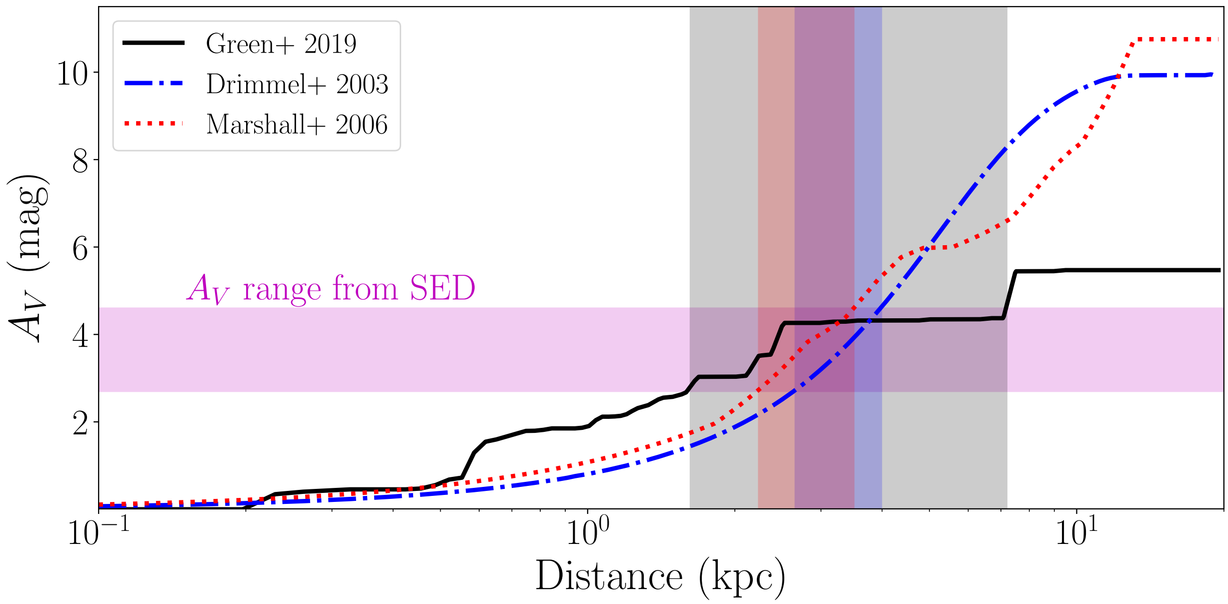

Figure 12: Constraints on the distance to ZTF SLRN-2020 using Galactic three dimensional dust extinction maps. We show the estimated dust extinction as a function of distance for three different extinction maps published in the literature[139–141]. We also show the 90% confidence interval for the estimated foreground extinction to ZTF SLRN-2020 based on our SED modeling as the magenta shaded region. For each dust extinction map, we show the allowed distance interval within the estimated extinction range with shaded vertical bars in the same color.

(created using the `mwdust` code[142]), the estimated A_V range inferred from the SED modeling as well as the allowed distance range for each map within the estimated A_V range. As shown, the different extinction maps are roughly consistent with each other within the estimated A_V range. Given the possible systematic differences between the different maps, we conservatively derive a distance range of $\approx 2-7$ kpc for the transient, placing this source well within the Galactic disk. As the distance ranges suggested by the different maps overlap consistently at a range of $\approx 3-4$ kpc, we nominally adopt 4 kpc as the best estimate for the source.

We use the distance and extinction estimate to derive the bolometric luminosity light curve of the optical transient around the peak of the outburst. We use the multi-color photometry from ZTF[6], binned in epochs of 3-days with coverage in all three (gri) filters, and fit a blackbody function to derive the effective temperature, luminosity and radius of the star for an estimated distance of 4 kpc. The fitting was performed by χ^2 minimization using the Markov Chain Monte Carlo fitting Python library `emcee`[88]. The results are shown in Figure 2. For comparison, we also show the evolution of the corresponding parameters for well studied red novae in the literature[8] as well as the $t^{-4/5}$ luminosity decay expected for the gravitational contraction of an inflated envelope surrounding the remnant[23]. We note that a foreground extinction significantly higher than the estimated interval ($A_V \gtrsim 5$ mag) would imply unphysically high blackbody temperatures ($>> 10^5$ K), corroborating the estimated extinction and distance range.

The bolometric luminosity of ZTF SLRN-2020 shows an initial plateau at $\approx 10^{35}$ erg s^{-1} for ≈ 15 days followed by a slow decline to 2×10^{34} erg s^{-1} over the next ≈ 100 days. We estimate the duration of the plateau by fitting the bolometric light curve with an analytical model developed for light curves of Type II supernovae[145] and previously used to model light curves of red novae[103]. The fitting was performed by χ^2 minimization using the `emcee` code, and suggests a best-fit plateau duration of $t_p = 25.6^{+5.6}_{-7.1}$ days as measured from the assumed time of eruption. The inferred bolometric luminosity from the `DUSTY` modeling at $\approx +120$ days after outburst peak is consistent with the bolometric fitting at the latest epochs, while the `DUSTY` modeling at $\approx +320$ days shows evidence of a plateau at very late phases.

[6]The ATLAS photometric filters cover very wide bandpasses over the g, r, and i bandpasses contemporaneously with the ZTF photometry, and hence we do use the c and o-band data for constructing bolometric light curves.

We estimate the total energy (E), luminosity (L_{90}) and duration (t_{90}) of the outburst[8] by performing trapezoidal integration on the bolometric light curve. We estimate uncertainties on these parameters by creating 1000 realizations of the bolometric luminosity light curve using the MCMC uncertainty intervals and then repeating the calculations. The corresponding estimates are $E \approx (6.5 \pm 1.7) \times 10^{41}$ erg, $L_{90} \approx (8.0 \pm 5.1) \times 10^{34}$ erg s^{-1} and $t_{90} \approx 103 \pm 20$ days for a distance of 4 kpc and foreground extinction of $A_V = 3.6$ mag. Although the t_{90} duration is found to be similar to the plateau duration (t_p) in previous objects[8], we find $t_{90} \approx 4 \times t_p$ likely due to a relatively small amount of unbound mass that contributes to the recombination luminosity on the plateau phase compared to the late-time gravitational contraction following the plateau. Considering the 68% confidence interval for the possible distance and foreground extinction, we find the total radiated energy and luminosity to be in the range $(1.0 - 12.1) \times 10^{41}$ erg s^{-1} and $(1.1 - 13.6) \times 10^{34}$ erg s^{-1}. In particular, even if the source was placed on the farthest side of the Galactic disk ($d \approx 20$ kpc), the estimated extinction would suggest a luminosity of $\lesssim 3.4 \times 10^{36}$ erg s^{-1}.

Progenitor photometry The progenitor of ZTF SLRN-2020 is detected only in the H and K filters of archival UKIRT images. Here, we attempt to constrain the progenitor star properties using the archival NIR photometry. In Figure 13, we show the position of the progenitor in the M_K vs. $H - K$ color magnitude diagram as a function of distance along the Galactic disk using different three dimensional dust extinction maps. To constrain the progenitor mass, we also show stellar evolutionary tracks for stars with initial masses ranging from $0.8 - 3.0\,M_\odot$ from the `MIST` database[146]. Figure 13 shows that the progenitor colors would be too blue to be consistent with any stellar tracks for distances larger than $\approx 8 - 10$ kpc as per the D03[139] and M06[140] models,

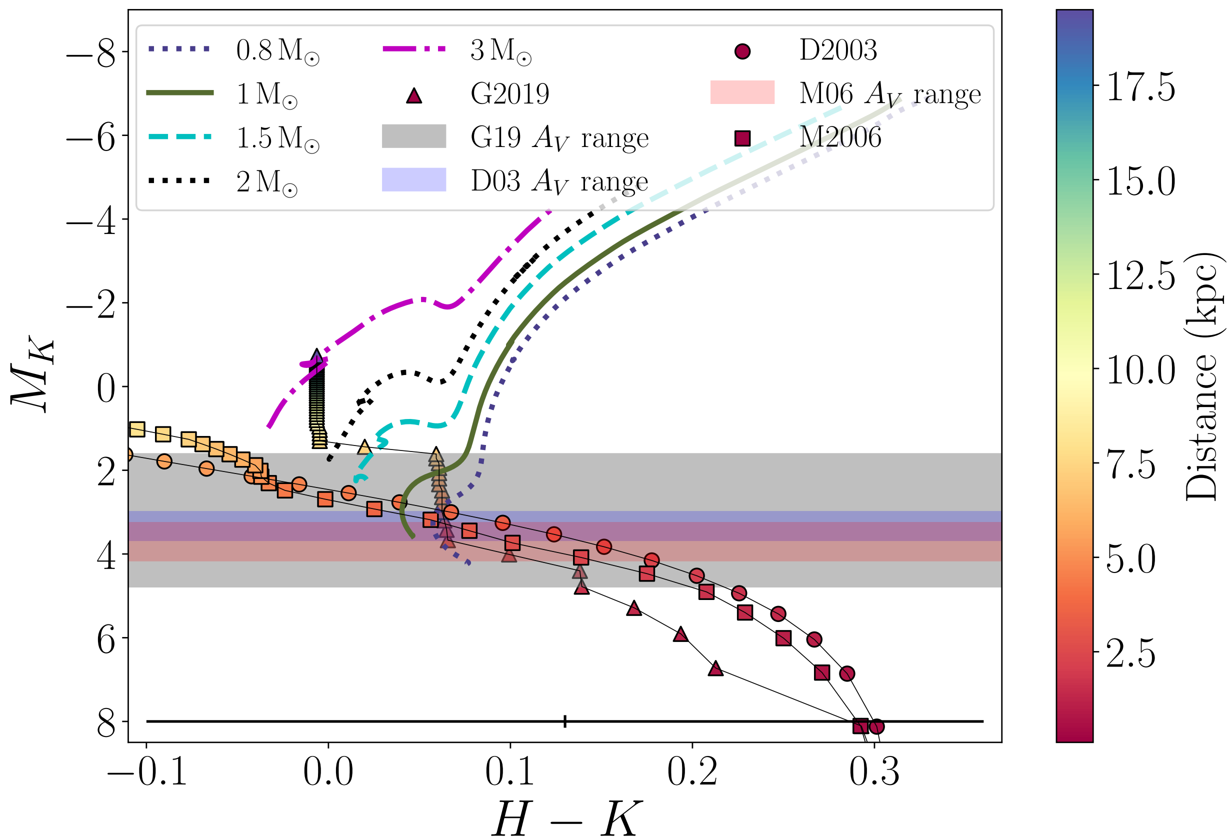

Figure 13: The progenitor of ZTF SLRN-2020 in the color magnitude diagram. For different distances along the Galactic disk, we use available three dimensional extinction maps to de-redden the progenitor photometry fluxes. The results are shown as circles for the D03[139] map, squares for the M06[140] map and as triangles for the G19[141] map. We also show the range of absolute magnitudes allowed by the 90% A_V confidence region (from the SED modeling) as blue, red and gray shaded regions respectively (see legend). We also plot stellar evolutionary tracks from the `MIST` database for stars of initial masses ranging from $0.8 - 3.0\,M_\odot$. The horizontal bar at the bottom shows the estimated uncertainty in the $H - K$ color.

consistent with our constraints on the distance based on the outburst SED modeling.

We find that the location of the progenitor within the estimated A_V range (shown as shaded region) is consistent with a $0.8 - 1.5\,M_\odot$ star on or evolving off the main sequence. Within the 90% confidence interval for the extinction, the photometric colors intersect the $1\,M_\odot$ stellar track at radii of $\approx 1 - 4\,\mathrm{R}_\odot$, which we adopt as the likely initial radius of the progenitor star. However, we are unable to further constrain the progenitor properties due to the large error on the photometric color. Specifically, the allowed progenitor flux and color are also consistent with a lower mass $\approx 0.8\,\mathrm{M}_\odot$progenitor star; in such a case, the engulfment would have occurred while the star was on the main sequence (given the current age of the Galactic disk population) likely driven by tidal interactions[38–40]. The late-time WIRC photometry together with the `DUSTY` modeling shows that the star has both nearly returned to its original photospheric temperature ($\approx 4000 - 5000\,$K; as suggested by the `DUSTY` model) while also having faded marginally below the progenitor brightness likely due to the optically thick dust shell surrounding the remnant.

Constraints on pre-outburst dust ZTF SLRN-2020 exhibits a mid-IR brightening in NEOWISE data starting $\approx 7\,$months prior to the optical outburst. Here, we use the pre-outburst brightening to constrain the evolution of the mass loss rate before the red nova outburst. In Figure 14, we show the evolution of the pre-outburst SED of the progenitor. The mid-IR source is clearly detected in both $W1$ and $W2$ bands $\approx 40\,$d prior to the optical outburst. We derive the dust temperature and mass by fitting the $W1$ and $W2$ photometry with a single-temperature modified blackbody represented by a Planck function multiplied by a grain efficiency factor (including effects of absorption and scattering). We use published values for silicate dust absorption and scattering[150].

We derive a dust temperature of $\approx 650\,$K and a dust mass of $M_d \approx (0.26 - 3.20) \times 10^{-6}\,\mathrm{M}_\odot$ over the distance range of $\approx 2 - 7\,$kpc at the $\approx -44\,$d epoch. The corresponding SED fits are shown in Figure 14. As the transient is only detected in the $W2$-band for the $\approx -244\,$d epoch, we estimate the dust mass at this epoch assuming the same dust temperature ($650\,$K; consistent

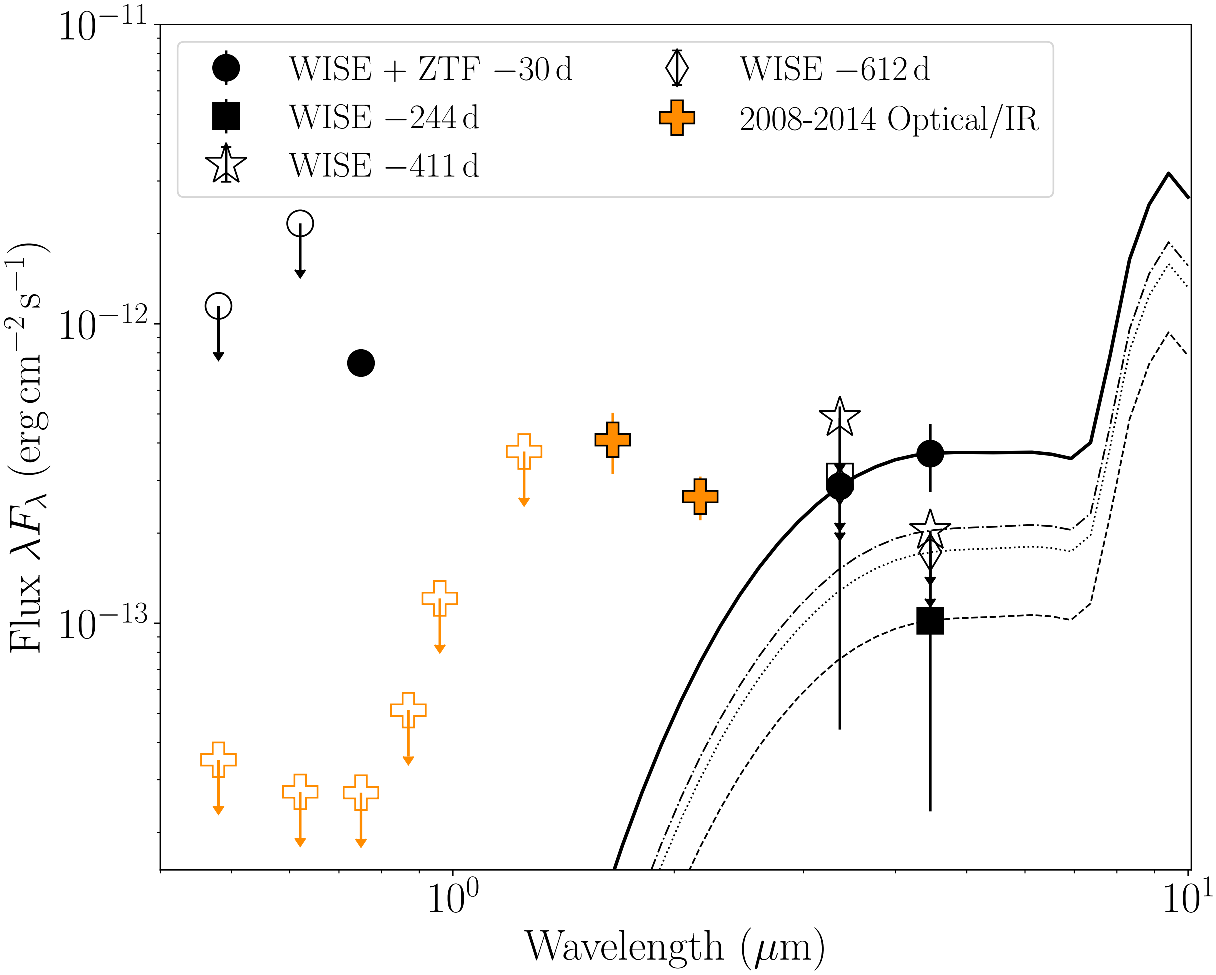

Figure 14: Evolution of the SED of ZTF SLRN-2020 progenitor prior to the onset of the optical transient. The orange points show the optical/IR photometry from $\approx 6 - 12$ years before the outburst. The black points show the evolution of the progenitor in the mid-IR starting ≈ 1.7 years before the transient. Solid points indicate detections while hollow points denote 3σ upper limits. For the -30 d and -244 d epochs, we show the best fit Silicate dust emission model fit using the mid-IR photometry (see text), while we show estimated upper limits to the dust emission using the $W2$ photometry. For the last epoch, we also show the pre-outburst optical brightening of the progenitor, coincident with the mid-IR source detected in NEOWISE.

with the $W1$ non-detection of the source) and use the $W2$ photometry to obtain a dust mass of $M_d \approx (0.7 - 8.8) \times 10^{-7}\,\mathrm{M}_\odot$. Instead, if we assume a lower dust temperature of $400\,\mathrm{K}$, the corresponding mass estimate is $(1.6 - 19) \times 10^{-6}\,\mathrm{M}_\odot$ that is unlikely as it is higher than the $-44\,\mathrm{d}$

epoch; we therefore nominally assume a temperature of 650 K. For prior epochs with no $W1$ or $W2$ detection, we only derive the maximum dust mass consistent with the NEOWISE non-detections; the SEDs fit to the NEOWISE non-detections suggest that the UKIRT NIR progenitor photometry ($\gtrsim 10$ years prior to outburst) is not affected by the mid-IR dust emission. The temporal evolution of dust mass is shown in Figure 4.

The transient also exhibits an optical brightening in i-band (compared to the archival PS1 limits), detected starting ≈ 40 d before the onset of the optical outburst. Figure 14 shows that the progenitor had brightened by $> 20\times$ in i-band since the non-detection in PS1; however, it cannot be explained as part of the thermal emission from the dust and likely arises from the stellar photosphere. The lack of multi-color photometry precludes constraints on the temperature and radius of the star during this phase. Similar behavior, arising out of expansion and cooling of the photosphere, or tidal heating prior to red nova outbursts has been suggested in V1309 Sco[28,30], M101-2015OT[128] and M31-LRN-2015[31,103]. Although we do not have extensive pre-outburst coverage in i-band where the brightening was detected, the plateau in optical luminosity prior to the outburst is strikingly similar to V838 Mon, M31-LRN-2015 and AT 2019zhd (Figure 6), where the constant luminosity has been attributed to ejected mass that is partially bound and forms a constant radius photosphere around the binary[20,23,103].

Observed rate estimates We estimate the observed rate of optical transients like ZTF SLRN-2020 by performing Monte Carlo simulations of the ZTF observing schedule together with a simulated population of ZTF SLRN-2020-like events in the Galactic plane. Our method draws from previous work on estimating rates of optical transients in ZTF [154] together with realistic methods for estimating the space distribution of Galactic plane outbursts[66]. We begin by constructing a template light curve for ZTF SLRN-2020 by fitting a Gaussian process model with a constant kernel to the peak-magnitude normalized light curve of ZTF SLRN-2020 in the r-band between phases of -20 d and 150 d from light curve peak. We do not include upper limits in the fitting process. We choose to perform this analysis only in r-band since the public survey data (where this transient was identified) includes only g and r band, while the fainter g-band light curve is poorly sampled at phases $\gtrsim 15$ days away from peak. The resulting template light curve is shown in Figure 15.

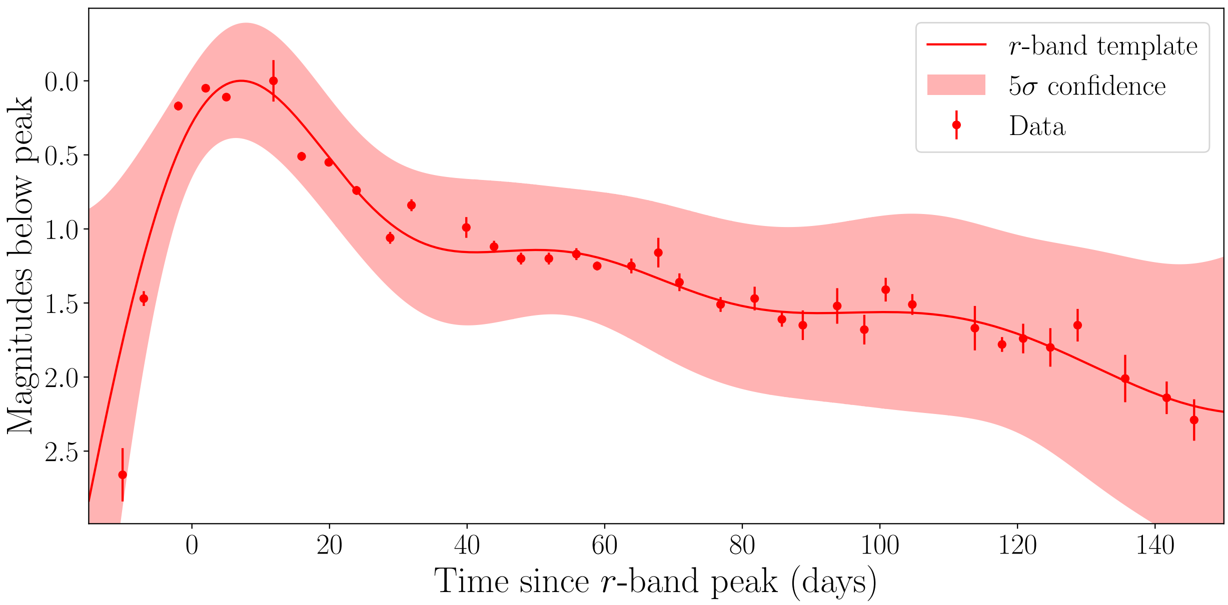

Figure 15: r-band template light curve of ZTF SLRN-2020, normalized to the peak magnitude of the outburst. The dots with error bars show the observed light curve while the red solid line and shaded region shows the best-fit template and its 5σ confidence interval.

Using the normalized light curve template, we simulate the observing schedule of the ZTF survey between the period of 2019-06-01 and 2021-11-30 (the period over which this search was performed). We assume that the probability of ZTF SLRN-2020-like outbursts follows the stellar mass density profile of the Milky Way and therefore simulate a population of transients following the density profile in [155] (their Table 1 and 2 for a contracted halo model). For each transient, we assume the outburst light curve follows the shape of the normalized template scaled to a peak absolute magnitude of $M_r = 2.0$ (as inferred for ZTF SLRN-2020) with a nominal scatter following a Gaussian distribution with standard deviation $\sigma = 0.5$ mag. Using the Galactic spatial location of each simulated transient, we estimate the apparent magnitude evolution as a function of light curve phase using three-dimensional dust distribution maps [141].

As in previous works[66], for each value of the Galactic event rate, we simulate a population of outbursts such that the number of events follows a Poisson distribution with a mean equal to the assumed rate. We perform 100 simulations for each value of the assumed rate, repeating the actual ZTF observation schedule to estimate the number of recovered events. Using the same selection criteria for long-lived Galactic plane outbursts as used to identify ZTF SLRN-2020, we calculate the median number of events that pass our selection criteria within this simulated sample, as well as its 68% confidence interval. Figure 16 shows the number of events expected to pass our filter as a function of the input Galactic rate. In order to derive the best-fit rate and its uncertainty given the one confirmed event in our search, we construct a distribution of the fraction of simulations that produce the one observed event as a function of the global rate. We fit a skewed normal function to this distribution to estimate a Galactic rate (with 68% confidence intervals)

$$r_0 = 4.3^{+7.5}_{-3.1}\,\mathrm{yr}^{-1} \tag{2}$$

where r_0 is the Galactic event rate. We show the best-fit distribution in Figure 16. However, we

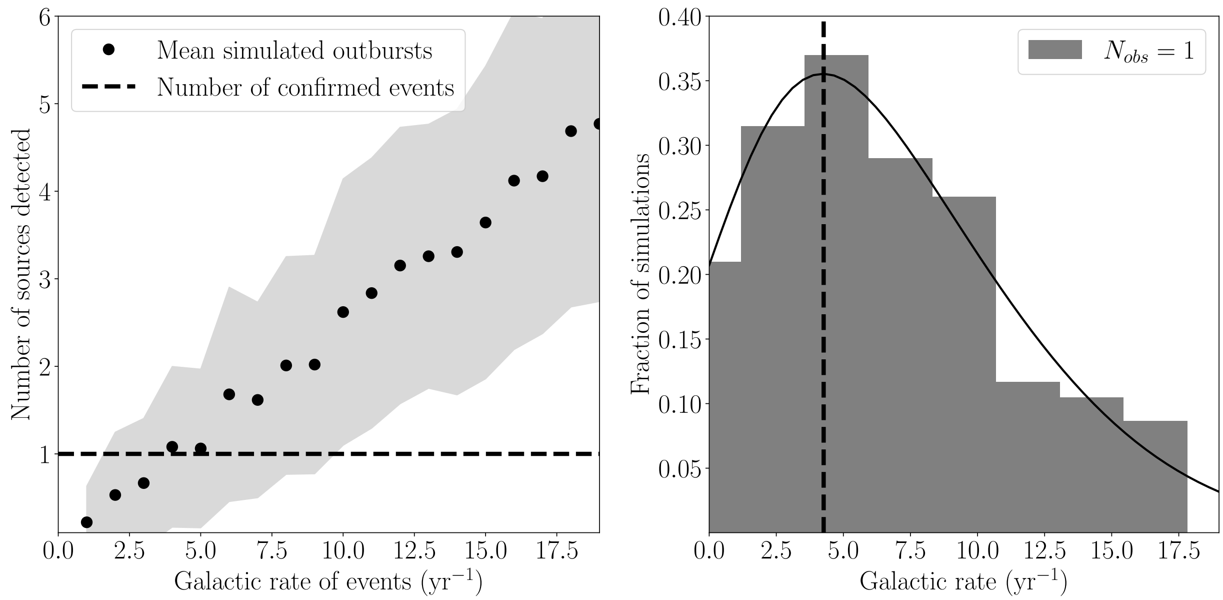

Figure 16: (Left) Number of simulated ZTF SLRN-2020-like events passing our selection criteria for an input Galactic rate of events and using the ZTF observing schedule during the search period. Black circles show the mean number of novae detected for an input rate while the shaded region corresponds to the measured 16-84th percentile range. (Right) Histogram of the fraction of simulations producing the number of confirmed events ($= 1$) as a function of the input Galactic rate. The distribution is fit with a skewed Gaussian function (shown as black solid line) and the dashed black line shows the best-fit peak of the distribution.

caution that i) the one observed event represents a lower limit to the actual number of events since it was not possible to obtain follow-up spectroscopy for all transients, ii) rate estimates from a single observed event are subject to large uncertainties and iii) the observed rates are subject to the recovery efficiency of the ZTF subtraction pipeline for faint transients in dense Galactic plane fields which have not been quantified for this simulation. Nevertheless, the observed rate estimate provides an order-of-magnitude estimate of the Galactic rate for comparison with theoretical estimates.

Light Curve Modeling and Interpretation ZTF SLRN-2020 has a uniquely low energy among the population of red novae transients. Here we discuss the interpertation of this light curve, with a focus on estimating the mass of the unseen companion object whose engulfment caused the red nova outburst. It is useful to compare ZTF SLRN-2020 to the properties of the particularly-well studied source V1309 Sco. Because of the extended period of pre-outburst eclipsing behavior in V1309 Sco, the system properties pre-merger are well known. The primary star of V1309 Sco was an $\approx 1.4 M_{\odot}$, $3.5 R_{\odot}$ sub giant[27], and the mass ratio was 0.094[29], implying a companion mass of $\approx 0.13 M_{\odot}$. The radiated energy was $\approx 3 \times 10^{44}$ erg. The outburst itself ejected an inferred $\approx 3 \times 10^{-2} M_{\odot}$ of material with an observed velocity of 150 km s^{-1}, about $1/3$ the surface escape velocity of the donor star [8].

By comparison, ZTF SLRN-2020 has very similar inferred primary star properties of $\approx 1\,\mathrm{M}_{\odot}$ and a likely radius of $1 - 4\,\mathrm{R}_{\odot}$. This association implies a similar primary star at a similar evolutionary state. The radiated energy of $\approx 6.5 \times 10^{41} (d/4\,\mathrm{kpc})^2$ erg represents a significantly less energetic coalescence than V1309 Sco. Similarly, the inferred ejecta mass is much lower than that of V1309 Sco at $\approx 3 \times 10^{-5}\,\mathrm{M}_{\odot}$ at $100\,\mathrm{km\,s}^{-1}$ during the plateau phase of the recombination-powered transient (Figure 4). In merger-powered transients, the loss of orbital energy powers the outburst. Thus, a characteristic energy scale is the gravitational binding energy of the pair separated by the donor star radius, $\Delta E_{\mathrm{orb}} \sim G M_1 M_2 / R_1$. Given that M_1 and R_1 are similar for V1309 Sco and ZTF SLRN-2020, we can use the observed energetics to trace the companion mass M_2. The radiated energy of ZTF SLRN-2020 is $\sim 10^2 - 10^3 \times$ lower than V1309 Sco. Similarly the ejecta mass (which is directly proportional to the events' kinetic energies given the similar system escape velocities) is $\sim 10^3\times$ lower in ZTF SLRN-2020 than that of V1309 Sco. Scaling down from the companion mass of $\approx 0.13 M_\odot$, these properties point to a planetary mass companion for ZTF SLRN-2020 with mass of 0.1 to 1 Jupiter-masses ($0.1 - 1 M_J$).

There are theoretical suggestions that the lower end of this mass range may be unrealistic. In particular, models of planet engulfment suggest that low-mass planets engulfed by their host stars may fall in so slowly that they do not produce appreciable disturbances or outbursts[5]. This indicates that the outburst properties might not scale linearly with companion mass down to a mass as low as $0.1 M_J$. Additionally, the association of this object with other, merger-powered red novae transients strongly suggests this scaled-down but otherwise identical physical process of engulfment of the companion. Among gaseous planets, lower-mass objects have lower density, such that a planet smaller than $\sim 1 M_J$ would be disrupted by tides outside of a solar-mass main sequence star[4,160] rather than plunging in to shock heat and eject stellar atmosphere material.

Constraints from Pre-Outburst Detections We can also draw information about the engulfment that occurred from the IR detections and limits in the years prior to the coalescence. We base these constraints on models of circumbinary mass loss in systems trending toward merger. These models have successfully explained the dynamics of orbital decay and the observations of increasing obscuration in V1309 Sco[28,30,32,162]. As the binary system approaches merger, mass loss near the outer, L_2 Lagrange point progressively drains angular momentum of the binary, causing it to tighten and further enhancing the mass transfer rate. We estimate the cumulative mass loss to the circumbinary environment based on the orbital change from the Roche limit separation, where mass exchange begins, to the point of engulfment, when the separation equals the donor radius. We use the RLOF software[163], which integrates the cumulative mass loss given coefficients of specific angular momentum loss motivated by hydrodynamic simulations of this process[32,36].

To do so, we must assume several parameters of the binary system. We have some constraints from the progenitor photometry to guide our choices. A nearly sun-like donor star (approximately $1M_\odot$ and 1 to $4R_\odot$) appears to be most consistent with the existing constraints. We adopt a $1M_\odot$ and $2R_\odot$ fiducial model, and compare to $1M_\odot$, $1R_\odot$ and $1M_\odot$, $4R_\odot$ examples to demonstrate the degree to which varying this within the uncertainty affects the result. We further assume that the structure of the star is approximated by a $\Gamma_{\rm s} = 4/3$ polytrope, that the gas adiabatic index is $\gamma = 5/3$ and that the star is not initially corotating with the companion orbit. These parameters each moderately affect the specific angular momentum loss that accompanies mass loss and orbital decay ($\sim 50\%$ differences in the predicted mass loss with varying parameters[32]). We then convert the estimated total mass lost to a dust mass assuming that the dust-to-gas mass ratio[134] is 5×10^{-3}.

A caveat is the extrapolation of these models to several orders of magnitude lower companion mass than the binary coalescences in which they have been tested. We caution, therefore, that if pre-outburst mass loss were caused by a different mechanism – like tidal heating of the stellar surface layers during increasingly rapid orbital decay – we might derive different estimates. These dust masses expected from modeled systems are shown in Figure 4. We see that the modeled dust masses and non-detections in the pre-outburst data are broadly consistent with a model that exhibits an exponentially increasing circumbinary distribution of gas and dust as it progresses toward merger. In overall normalization, our curves are most consistent with a mass ratio of $q \approx$

10^{-3} to 10^{-1}, implying a companion mass of $\sim 10^{-2} M_{\odot}$, or $10 M_J$. This mass is larger than the mass inferred from the recombination powered transient's mass and energy budget, as discussed above. However, both mass estimates are strongly suggestive of a planetary mass companion object producing the ZTF SLRN-2020 transient.

Understanding a Planetary Engulfment The planetary mass range inferred from various lines of evidence points to the fact that ZTF SLRN-2020 probes new parameter space among the red novae. Hydrodynamic simulations of stellar coalescence have suggested that as the mass ratio decreases, a smaller fraction of the shock-heated material is truly unbound from the system and ejected [35,36]. The remaining, bound material settles into a shock-heated, rotating envelope in which spiral shocks play an important role in redistributing energy and angular momentum[36]. An extension of this is the limit that the smallest companions should be too insignificant to eject any mass from the host star when they are engulfed. Thus, we suggest that the combination of pre-cursor and lightcurve data shown in Figure 4 are indicative of a system in which the majority of the shock-heated stellar atmosphere remains bound. Indeed, this is strongly suggested by inferred velocities in Figure 4, which are much less than the local escape velocity at 3×10^{11} cm of $\approx 300\,\mathrm{km\,s^{-1}}$.

If most of the stellar atmosphere mass remains bound following the engulfment, this would attribute the plateau luminosity to the recombination of a comparatively small unbound mass fraction ($\approx 3 \times 10^{-5} M_{\odot}$). It also informs our understanding of the brightness and colors of ZTF SLRN-2020 over the hundred-day observing window. ZTF SLRN-2020's temperature remains higher than other red novae and its photosphere radius, following its initial expansion to $\approx 3 \times 10^{11}\,\mathrm{cm} \approx 4.3\,\mathrm{R}_{\odot}$, gradually decreases rather than growing. These trends both indicate that following an initial period of mass ejection, we may be witnessing the hydrodynamic and thermal relaxation of still-bound stellar material that has been disturbed by the engulfment of the substellar companion. Indeed, the late-time light curve follows a roughly $t^{-4/5}$ power-law, which is consistent with observations of other merger remnants[23].

We note that the small ejected mass is consistent with the non-detection of molecular line emission in the SMA and VLA observations. While a detailed molecular excitation analysis is beyond the scope of the work given the non-detection, we can interpret these data with comparisons to the molecular line observations of V1309 Sco[166]. Observations with the Atacama Large Millimeter Array detected the 230 GHz CO transition in V1309 Sco ≈ 8 years after merger at a flux level of $\approx 3.3\,\mathrm{Jy\,km\,s^{-1}}$ (peak line flux of $\approx 13\,\mathrm{mJy}$ for the measured line width of $\sigma \approx 100\,\mathrm{km\,s^{-1}}$). As the distance to V1309 Sco[9] is similar to that estimated for ZTF SLRN-2020, and assuming similar molecular excitation conditions as in V1309 Sco, we estimate that the relevant line flux in ZTF SLRN-2020 would be $\approx 10^{-3}\times$ V1309 Sco (peak line flux of $\lesssim 0.02\,\mathrm{mJy}$) if the molecular line fluxes scale approximately linearly with the inferred mass of the unbound material (Figure 4). Noting that ZTF SLRN-2020 was observed at a much earlier phase and therefore may have different excitation conditions, the non-detection of molecular emission is consistent with the small inferred ejecta mass in the eruption. While SiO maser emission at 43 GHz was only detected for V838 Mon[167,168], we use similar scaling arguments and accounting for the larger distance to V838 Mon, we estimate the maser line flux in ZTF SLRN-2020 to be $\sim 10^{-4}\times$ fainter ($\lesssim 0.5\,\mathrm{mJy}$ at peak for a resolution of $\approx 0.5\,\mathrm{km\,s^{-1}}$) and hence consistent with the non-detection ($\lesssim 6\,\mathrm{mJy}$).

The upper end of the range of mass possibilities for the companion of ZTF SLRN-2020 nears the mass range of brown dwarfs, which extends from roughly $13M_J$ to $80M_J$. Could ZTF SLRN-2020's companion object be a brown dwarf rather than a giant planet? We suggest that this is substantially less likely because brown dwarf companions at similar separations to hot Jupiters are nearly an order of magnitude more rare[2]. The close-companion portion of this "brown dwarf desert" may be caused by the more-rapid tidal decay of these objects orbits into their host stars: even if these objects were formed at similar rates to hot Jupiters, many would coalesce with their host stars during the pre-main sequence. Since ZTF SLRN-2020 shows no evidence of being a young star there seems to be substantially more support for a planetary companion.

Theoretical Planetary Engulfment Event Rates Planets and substellar objects decay toward merger with their host stars through a combination of tidal orbital decay (due to asynchronous rotation of the host star with the companion orbit) and stellar evolution (which increases the radius of the host star while lowering its spin rate)[39]. The currently observed population of hot Jupiter exoplanets all have inferred tidal decay times of less than 10^{10} yr. Tidal decay has been directly detected for WASP 12b[41,42,170,171]. Even without tidal decay, each of these planets will surely merge with its host star as these stars increase in radius on the sub giant and giant branches.

There are uncertainties in the propogation of this observed distribution to an engulfment event rate. As Metzger et al[4] have noted, the distribution of known planets at the closest separations implies a much higher coalescence rate than the apparent number at larger separations (see their Figure 1). This points to a need to resupply planets to these close-in orbits to maintain the currently-observed distribution. The occurrence of very close, Jupiter-like planets implies a coalescence rate of ~ 0.1 yr^{-1} in the galaxy[4], while the number of hot Jupiters at slightly larger separations (with tidal decay timescales of 10^9 to 10^{10}) appears to be fewer. Whether this relates to observational selection effects or is an intrinsic property of the population is currently under discussion[171].

With these caveats in mind, we can produce an order of magnitude estimate of the giant-planet engulfment rate as follows. The total mass of stars in the Milky Way is $\sim 6.4 \times 10^{10} M_{\odot}$[174]. In a Salpeter IMF, approximately 1/3 of this mass comes from stars greater than a solar mass (which is roughly the fraction that evolve off of the main sequence in less than 10^{10} yr). This implies that roughly 10^{10} stars have evolved off of the main sequence in the history of the galaxy. If 1% of these stars hosted hot Jupiters[2,175], then the time-averaged event rate would be $(10^8/10^{10}\text{yr}) \sim 10^{-2}$ yr^{-1}. In reality, this time-averaged estimate represents a lower limit because it does not account for the apparent resupply of planets to close in orbits, perhaps through dynamical scatterings (for example, Stephan et al[176] estimate an engulfment rate of 0.1 yr^{-1} from A-type stars alone). The normalization of these theoretical rates suggests that the detection of a giant planet engulfment by ZTF is perhaps fortunate, but not extremely unlikely. On the other hand, observational constraints on this rate through transient discoveries may soon provide important insights into the architecture and evolution of extrasolar planetary systems.

A Missing Link in Star–Planet Coevolution As the existence of exoplanetary systems have become increasingly clear[2], the discovery of a planetary engulfment event has been long-awaited. There have been numerous theoretical predictions of the multi-wavelength signatures of these events as they occur[4,5,34,178,179]. In particular, predictions have focused on their possible appearance as optical transients, but many have over-estimated the luminosity and underestimated the event duration relative to ZTF SLRN-2020, because they have imagined fast ejecta moving at similar to the stellar escape velocity. A notable exception comes from Yamazaki et al[178], whose predictions for emission from a shock-heated plasma bubble show characteristic temperatures, photosphere radii, and peak luminosities very similar to those observed in ZTF SLRN-2020, strengthening the interpretation of a small quantity of shock-heated mass powering the early emission. More detailed comparison of this range of models to ZTF SLRN-2020's emerging properties will be crucial to guide future search efforts. In particular, ZTF SLRN-2020's high IR luminosity (relative to the optical bands) suggests that searching for similar events in the IR bands may be much more fruitful than in the optical.

An even larger body of effort has been devoted to understanding the long-lasting effects of substellar engulfment[6,52,53], with the motivation that if a large fraction of stars engulf one or more planets as they evolve, perhaps these events leave long-lasting impacts on the observable stellar characteristics. One possible property that has been invoked is secular declines in luminosity, which might trace the cooling of a star following the mechanical addition of heat from an engulfment[5,48]. Another is enrichment of the stellar atmosphere by lithium and other elements carried by the planet bulk composition in higher abundance than the star[53]. Lithium is thought to be a particularly useful tracer because its fragile structure is dissociated in stars, but persists in substellar objects[6,50–52]. Observations of the remnant of ZTF SLRN-2020 at relatively high spectral resolution could search for signs of lithium enrichment and serve as a useful benchmark for these theories, as well as compare to recent studies of other red novae remnants[186]. A final possible signature that has been extensively considered is stellar rotation, with enhancements in otherwise-slow rotation rates thought to be be possible due to the deposition of angular momentum as the planet is engulfed[55–57].

Since the total angular momentum budget of a substellar engulfment is well-known, the impact on the observable spin rate (as well as the evolution of that spin rate) becomes deeply revealing about the transport of angular momentum in the stellar interior. As future work traces each of these properties in ZTF SLRN-2020 and similar future transients, we anticipate that these events will serve as a crucial missing link in connecting the properties of observed planetary systems to the transients they produce and their effects on their host stars.

Table 1: Optical/NIR photometry of ZTF SLRN-2020 in the AB magnitude system.

MJD	Phase (d)	Filter	Mag	Instrument
58955.44	-38.95	r	> 19.70	P48+ZTF
58972.44	-21.95	r	> 20.41	P48+ZTF
58975.46	-18.93	r	> 20.14	P48+ZTF
58978.49	-15.90	r	> 20.25	P48+ZTF
58983.38	-11.01	r	20.56 ± 0.18	P48+ZTF
58986.46	-7.93	r	19.37 ± 0.05	P48+ZTF
58991.48	-2.91	r	18.07 ± 0.03	P48+ZTF
58995.46	1.07	r	17.95 ± 0.01	P48+ZTF
58998.46	4.07	r	18.01 ± 0.02	P48+ZTF
59005.31	10.92	r	17.90 ± 0.14	P48+ZTF
59009.40	15.01	r	18.41 ± 0.03	P48+ZTF
59013.35	18.96	r	18.45 ± 0.02	P48+ZTF
59017.39	23.00	r	18.64 ± 0.03	P48+ZTF
59022.27	27.88	r	18.96 ± 0.04	P48+ZTF
59025.37	30.98	r	18.74 ± 0.04	P48+ZTF
59033.34	38.95	r	18.89 ± 0.07	P48+ZTF
59037.37	42.98	r	19.02 ± 0.04	P48+ZTF
59041.29	46.90	r	19.10 ± 0.04	P48+ZTF
59045.34	50.95	r	19.10 ± 0.04	P48+ZTF

Table 1: Photometry of ZTF SLRN-2020 in the optical and NIR bands (continued).

MJD	Phase (d)	Filter	Mag	Instrument
59049.34	54.95	r	19.07 ± 0.04	P48+ZTF
59052.36	57.97	r	19.15 ± 0.03	P48+ZTF
59057.33	62.94	r	19.15 ± 0.05	P48+ZTF
59061.25	66.86	r	19.06 ± 0.10	P48+ZTF
59064.32	69.93	r	19.26 ± 0.06	P48+ZTF
59070.30	75.91	r	19.41 ± 0.05	P48+ZTF
59075.25	80.86	r	19.37 ± 0.08	P48+ZTF
59079.21	84.82	r	19.51 ± 0.05	P48+ZTF
59082.25	87.86	r	19.55 ± 0.10	P48+ZTF
59087.25	92.86	r	19.42 ± 0.12	P48+ZTF
59091.19	96.80	r	19.58 ± 0.10	P48+ZTF
59094.30	99.91	r	19.31 ± 0.08	P48+ZTF
59098.17	103.78	r	19.41 ± 0.07	P48+ZTF
59107.26	112.87	r	19.57 ± 0.15	P48+ZTF
59111.21	116.82	r	19.68 ± 0.05	P48+ZTF
59114.28	119.89	r	19.64 ± 0.10	P48+ZTF
59118.23	123.84	r	19.70 ± 0.13	P48+ZTF
59122.20	127.81	r	19.55 ± 0.11	P48+ZTF
59129.11	134.72	r	19.91 ± 0.16	P48+ZTF

Table 1: Photometry of ZTF SLRN-2020 in the optical and NIR bands (continued).

MJD	Phase (d)	Filter	Mag	Instrument
59135.14	140.75	r	20.04 ± 0.11	P48+ZTF
59139.13	144.74	r	20.19 ± 0.14	P48+ZTF
59146.11	151.72	r	20.26 ± 0.26	P48+ZTF
59151.10	156.71	r	20.17 ± 0.21	P48+ZTF
59155.08	160.69	r	> 18.01	P48+ZTF
59164.12	169.73	r	19.86 ± 0.26	P48+ZTF
59169.14	174.75	r	20.08 ± 0.19	P48+ZTF
59182.07	187.68	r	20.14 ± 0.15	P48+ZTF
59185.08	190.69	r	20.08 ± 0.12	P48+ZTF
59188.08	193.69	r	20.27 ± 0.15	P48+ZTF
59194.07	199.68	r	> 19.84	P48+ZTF
59248.56	254.17	r	20.88 ± 0.28	P48+ZTF
59251.57	257.18	r	20.62 ± 0.22	P48+ZTF
59254.57	260.18	r	20.53 ± 0.22	P48+ZTF
59264.54	270.15	r	20.76 ± 0.14	P48+ZTF
59267.54	273.15	r	21.12 ± 0.14	P48+ZTF
59320.48	326.09	r	21.02 ± 0.29	P48+ZTF
59373.39	379.00	r	21.25 ± 0.32	P48+ZTF
58944.48	-49.91	g	> 19.96	P48+ZTF

Table 1: Photometry of ZTF SLRN-2020 in the optical and NIR bands (continued).

MJD	Phase (d)	Filter	Mag	Instrument
58955.48	-38.91	g	> 20.38	P48+ZTF
58963.40	-30.99	g	> 21.60	P48+ZTF
58966.46	-27.93	g	> 21.38	P48+ZTF
58974.48	-19.91	g	> 20.87	P48+ZTF
58978.42	-15.97	g	> 20.66	P48+ZTF
58986.41	-7.98	g	21.41 ± 0.16	P48+ZTF
58991.40	-2.99	g	19.87 ± 0.05	P48+ZTF
58994.43	0.04	g	19.78 ± 0.04	P48+ZTF
58998.42	4.03	g	19.83 ± 0.05	P48+ZTF
59002.46	8.07	g	19.89 ± 0.09	P48+ZTF
59012.33	17.94	g	20.34 ± 0.07	P48+ZTF
59016.36	21.97	g	20.72 ± 0.08	P48+ZTF
59020.39	26.00	g	20.74 ± 0.09	P48+ZTF
59024.36	29.97	g	20.65 ± 0.11	P48+ZTF
59028.36	33.97	g	20.85 ± 0.18	P48+ZTF
59034.25	39.86	g	> 19.92	P48+ZTF
59037.25	42.86	g	> 20.22	P48+ZTF
59040.27	45.88	g	21.03 ± 0.13	P48+ZTF
59043.35	48.96	g	20.97 ± 0.09	P48+ZTF

Table 1: Photometry of ZTF SLRN-2020 in the optical and NIR bands (continued).

MJD	Phase (d)	Filter	Mag	Instrument
59048.36	53.97	g	21.11 ± 0.15	P48+ZTF
59052.29	57.90	g	21.00 ± 0.10	P48+ZTF
59055.29	60.90	g	21.29 ± 0.18	P48+ZTF
59060.38	65.99	g	20.92 ± 0.19	P48+ZTF
59064.22	69.83	g	> 20.34	P48+ZTF
59067.32	72.93	g	21.52 ± 0.25	P48+ZTF
59072.23	77.84	g	21.49 ± 0.21	P48+ZTF
59076.27	81.88	g	21.37 ± 0.19	P48+ZTF
59080.21	85.82	g	21.11 ± 0.21	P48+ZTF
59084.19	89.80	g	21.47 ± 0.22	P48+ZTF
59091.23	96.84	g	> 20.68	P48+ZTF
59095.21	100.82	g	> 20.74	P48+ZTF
59098.21	103.82	g	21.36 ± 0.21	P48+ZTF
59107.17	112.78	g	> 20.52	P48+ZTF
59111.13	116.74	g	21.61 ± 0.20	P48+ZTF
59114.21	119.82	g	> 21.00	P48+ZTF
59117.23	122.84	g	> 20.32	P48+ZTF
59121.17	126.78	g	> 20.40	P48+ZTF
59125.17	130.78	g	> 20.02	P48+ZTF

Table 1: Photometry of ZTF SLRN-2020 in the optical and NIR bands (continued).

MJD	Phase (d)	Filter	Mag	Instrument
59131.17	136.78	g	> 20.26	P48+ZTF
59135.12	140.73	g	> 21.24	P48+ZTF
59139.11	144.72	g	> 21.07	P48+ZTF
59146.13	151.74	g	> 18.03	P48+ZTF
59149.18	154.79	g	> 20.02	P48+ZTF
59153.13	158.74	g	> 20.12	P48+ZTF
59157.15	162.76	g	> 19.88	P48+ZTF
59167.14	172.75	g	> 20.53	P48+ZTF
59171.13	176.74	g	> 20.38	P48+ZTF
58962.43	-31.96	i	20.65 ± 0.26	P48+ZTF
58964.49	-29.90	i	20.41 ± 0.09	P48+ZTF
58968.49	-25.90	i	20.48 ± 0.16	P48+ZTF
58971.47	-22.92	i	20.53 ± 0.17	P48+ZTF
58972.49	-21.90	i	20.57 ± 0.17	P48+ZTF
58976.43	-17.96	i	20.13 ± 0.16	P48+ZTF
58983.40	-10.99	i	19.56 ± 0.18	P48+ZTF
58985.37	-9.02	i	18.38 ± 0.03	P48+ZTF
58991.38	-3.01	i	17.08 ± 0.02	P48+ZTF
58994.39	0.00	i	17.06 ± 0.02	P48+ZTF

Table 1: Photometry of ZTF SLRN-2020 in the optical and IR bands (continued).

MJD	Phase (d)	Filter	Mag	Instrument
58996.41	2.02	i	17.06 ± 0.04	P48+ZTF
58997.37	2.98	i	17.13 ± 0.04	P48+ZTF
59001.35	6.96	i	17.18 ± 0.05	P48+ZTF
59004.37	9.98	i	17.30 ± 0.05	P48+ZTF
59005.39	11.00	i	17.57 ± 0.11	P48+ZTF
59008.46	14.07	i	17.54 ± 0.05	P48+ZTF
59009.34	14.95	i	17.54 ± 0.03	P48+ZTF
59012.47	18.08	i	17.53 ± 0.02	P48+ZTF
59017.35	22.96	i	17.61 ± 0.05	P48+ZTF
59018.33	23.94	i	17.77 ± 0.03	P48+ZTF
59022.33	27.94	i	17.87 ± 0.02	P48+ZTF
59026.33	31.94	i	17.78 ± 0.02	P48+ZTF
59031.31	36.92	i	18.01 ± 0.05	P48+ZTF
59032.29	37.90	i	18.02 ± 0.03	P48+ZTF
59035.29	40.90	i	18.00 ± 0.08	P48+ZTF
59036.35	41.96	i	18.00 ± 0.02	P48+ZTF
59040.35	45.96	i	18.08 ± 0.04	P48+ZTF
59042.27	47.88	i	18.11 ± 0.03	P48+ZTF
59045.32	50.93	i	18.11 ± 0.04	P48+ZTF

1 Data Availability

2 Code Availability

The first author will provide python code used to analyze the observations, and any data used to generate figures, upon request.

References

62. Bellm, E. C. *et al.* The Zwicky Transient Facility: System Overview, Performance, and First Results. PASP **131**, 018002 (2019). 1902.01932.

63. Graham, M. J. *et al.* The Zwicky Transient Facility: Science Objectives. PASP **131**, 078001 (2019). 1902.01945.

64. Dekany, R. *et al.* The Zwicky Transient Facility: Observing System. PASP **132**, 038001 (2020). 2008.04923.

65. Bellm, E. C. *et al.* The Zwicky Transient Facility: Surveys and Scheduler. PASP **131**, 068003 (2019). 1905.02209.

66. De, K. *et al.* A Population of Heavily Reddened, Optically Missed Novae from Palomar Gattini-IR: Constraints on the Galactic Nova Rate. ApJ **912**, 19 (2021). 2101.04045.

67. Duev, D. A. *et al.* Real-bogus classification for the Zwicky Transient Facility using deep learning. MNRAS **489**, 3582–3590 (2019). 1907.11259.

Table 1: Photometry of ZTF SLRN-2020 in the optical and IR bands (continued).

MJD	Phase (d)	Filter	Mag	Instrument
59047.30	52.91	i	18.17 ± 0.06	P48+ZTF
59060.28	65.89	i	18.22 ± 0.04	P48+ZTF
59068.31	73.92	i	18.36 ± 0.04	P48+ZTF
59070.27	75.88	i	18.45 ± 0.03	P48+ZTF
59073.27	78.88	i	18.48 ± 0.07	P48+ZTF
59075.29	80.90	i	18.43 ± 0.06	P48+ZTF
59076.26	81.87	i	18.49 ± 0.08	P48+ZTF
59079.25	84.86	i	18.53 ± 0.04	P48+ZTF
59085.29	90.90	i	18.54 ± 0.05	P48+ZTF
59087.23	92.84	i	18.45 ± 0.03	P48+ZTF
59091.18	96.79	i	18.41 ± 0.03	P48+ZTF
59094.25	99.86	i	18.38 ± 0.10	P48+ZTF
59095.23	100.84	i	18.41 ± 0.03	P48+ZTF
59098.23	103.84	i	18.44 ± 0.05	P48+ZTF
59106.17	111.78	i	18.57 ± 0.05	P48+ZTF
59110.19	115.80	i	18.59 ± 0.04	P48+ZTF
59112.21	117.82	i	18.67 ± 0.06	P48+ZTF
59112.27	117.88	i	18.64 ± 0.07	P48+ZTF
59114.17	119.78	i	18.65 ± 0.07	P48+ZTF

Table 1: Photometry of ZTF SLRN-2020 in the optical and IR bands (continued).

MJD	Phase (d)	Filter	Mag	Instrument
59116.18	121.79	i	18.65 ± 0.06	P48+ZTF
59118.17	123.78	i	18.68 ± 0.03	P48+ZTF
59121.12	126.73	i	18.70 ± 0.08	P48+ZTF
59121.13	126.74	i	18.70 ± 0.03	P48+ZTF
59125.13	130.74	i	18.79 ± 0.07	P48+ZTF
59125.14	130.75	i	18.77 ± 0.03	P48+ZTF
59128.19	133.80	i	18.89 ± 0.08	P48+ZTF
59128.22	133.83	i	18.84 ± 0.05	P48+ZTF
59137.00	142.61	i	19.16 ± 0.02	P48+ZTF
58958.58	-35.81	c	> 20.53	ATLAS
58966.52	-27.87	c	> 20.29	ATLAS
58970.57	-23.82	c	> 20.01	ATLAS
58990.48	-3.91	c	19.12 ± 0.05	ATLAS
58994.47	0.08	c	18.81 ± 0.05	ATLAS
58998.47	4.08	c	18.88 ± 0.05	ATLAS
59022.45	28.06	c	20.23 ± 0.20	ATLAS
59026.48	32.09	c	19.75 ± 0.10	ATLAS
59050.41	56.02	c	20.45 ± 0.20	ATLAS
59054.48	60.09	c	> 19.88	ATLAS

Table 1: Photometry of ZTF SLRN-2020 in the optical and IR bands (continued).

MJD	Phase (d)	Filter	Mag	Instrument
59071.35	76.96	c	20.55 ± 0.28	ATLAS
59074.41	80.02	c	20.35 ± 0.17	ATLAS
59078.34	83.95	c	20.19 ± 0.19	ATLAS
59082.33	87.94	c	20.52 ± 0.25	ATLAS
59102.30	107.91	c	20.48 ± 0.16	ATLAS
59106.32	111.93	c	20.66 ± 0.24	ATLAS
59110.27	115.88	c	20.38 ± 0.24	ATLAS
59130.31	135.92	c	20.95 ± 0.25	ATLAS
59138.28	143.89	c	> 20.32	ATLAS
59142.22	147.83	c	> 20.23	ATLAS
58944.60	-49.79	o	> 19.10	ATLAS
58949.48	-44.91	o	> 19.42	ATLAS
58956.59	-37.80	o	> 19.86	ATLAS
58960.62	-33.77	o	> 19.93	ATLAS
58964.54	-29.85	o	> 19.43	ATLAS
58968.53	-25.86	o	> 19.96	ATLAS
58972.51	-21.88	o	> 20.15	ATLAS
58976.54	-17.85	o	> 19.58	ATLAS
58980.49	-13.90	o	> 19.68	ATLAS

Table 1: Photometry of ZTF SLRN-2020 in the optical and IR bands (continued).

MJD	Phase (d)	Filter	Mag	Instrument
58984.58	-9.81	o	19.45 ± 0.06	ATLAS
58988.47	-5.92	o	18.41 ± 0.04	ATLAS
58992.50	-1.89	o	17.63 ± 0.02	ATLAS
58996.55	2.16	o	17.67 ± 0.10	ATLAS
59000.46	6.07	o	17.79 ± 0.02	ATLAS
59004.41	10.02	o	18.01 ± 0.03	ATLAS
59008.59	14.20	o	18.18 ± 0.05	ATLAS
59016.44	22.05	o	18.22 ± 0.07	ATLAS
59020.39	26.00	o	18.45 ± 0.05	ATLAS
59024.34	29.95	o	18.45 ± 0.04	ATLAS
59028.44	34.05	o	18.54 ± 0.04	ATLAS
59031.47	37.08	o	18.72 ± 0.05	ATLAS
59036.49	42.10	o	18.67 ± 0.05	ATLAS
59040.53	46.14	o	18.91 ± 0.06	ATLAS
59044.43	50.04	o	18.79 ± 0.08	ATLAS
59048.41	54.02	o	18.82 ± 0.06	ATLAS
59052.45	58.06	o	18.77 ± 0.06	ATLAS
59058.33	63.94	o	18.75 ± 0.04	ATLAS
59061.34	66.95	o	18.94 ± 0.12	ATLAS

Table 1: Photometry of ZTF SLRN-2020 in the optical and IR bands (continued).

MJD	Phase (d)	Filter	Mag	Instrument
59064.42	70.03	o	18.86 ± 0.13	ATLAS
59068.42	74.03	o	18.96 ± 0.06	ATLAS
59072.44	78.05	o	18.96 ± 0.08	ATLAS
59076.40	82.01	o	18.99 ± 0.07	ATLAS
59080.36	85.97	o	19.25 ± 0.07	ATLAS
59084.33	89.94	o	19.19 ± 0.06	ATLAS
59088.34	93.95	o	19.30 ± 0.12	ATLAS
59092.33	97.94	o	19.27 ± 0.13	ATLAS
59096.36	101.97	o	19.02 ± 0.06	ATLAS
59100.30	105.91	o	19.22 ± 0.08	ATLAS
59104.33	109.94	o	19.23 ± 0.09	ATLAS
59108.29	113.90	o	19.36 ± 0.10	ATLAS
59112.28	117.89	o	19.36 ± 0.10	ATLAS
59115.34	120.95	o	19.42 ± 0.11	ATLAS
59120.32	125.93	o	19.19 ± 0.14	ATLAS
59126.25	131.86	o	19.74 ± 0.14	ATLAS
59129.27	134.88	o	19.39 ± 0.12	ATLAS
59136.28	141.89	o	19.71 ± 0.18	ATLAS
59140.23	145.84	o	19.58 ± 0.14	ATLAS

68. Chambers, K. C. *et al.* The Pan-STARRS1 Surveys. *arXiv e-prints* arXiv:1612.05560 (2016). 1612.05560.

69. Kawash, A. *et al.* Classical Novae Masquerading as Dwarf Novae? Outburst Properties of Cataclysmic Variables with ASAS-SN. ApJ **910**, 120 (2021). 2101.12239.

70. Masci, F. J. *et al.* The Zwicky Transient Facility: Data Processing, Products, and Archive. PASP **131**, 018003 (2019). 1902.01872.

71. Zackay, B., Ofek, E. O. & Gal-Yam, A. Proper Image Subtraction - Optimal Transient Detection, Photometry, and Hypothesis Testing. ApJ **830**, 27 (2016). 1601.02655.

72. Tonry, J. L. *et al.* ATLAS: A High-cadence All-sky Survey System. PASP **130**, 064505 (2018). 1802.00879.

73. Wright, E. L. *et al.* The Wide-field Infrared Survey Explorer (WISE): Mission Description and Initial On-orbit Performance. AJ **140**, 1868–1881 (2010). 1008.0031.

74. Mainzer, A. *et al.* Initial Performance of the NEOWISE Reactivation Mission. ApJ **792**, 30 (2014). 1406.6025.

75. Lang, D. unWISE: Unblurred Coadds of the WISE Imaging. AJ **147**, 108 (2014). 1405.0308.

76. Meisner, A. M., Lang, D. & Schlegel, D. J. Time-resolved WISE/NEOWISE Coadds. AJ **156**, 69 (2018). 1710.02526.

77. De, K. *et al.* Palomar Gattini-IR: Survey Overview, Data Processing System, On-sky Performance and First Results. PASP **132**, 025001 (2020). `1910.13319`.

78. Burrows, D. N. *et al.* The Swift X-Ray Telescope. *Space Science Reviews* **120**, 165–195 (2005). `astro-ph/0508071`.

79. Gehrels, N. *et al.* The Swift Gamma-Ray Burst Mission. ApJ **611**, 1005–1020 (2004). `astro-ph/0405233`.

80. Roming, P. W. A. *et al.* The Swift Ultra-Violet/Optical Telescope. Space Sci. Rev. **120**, 95–142 (2005). `astro-ph/0507413`.

81. Corral-Santana, J. M. *et al.* BlackCAT: A catalogue of stellar-mass black holes in X-ray transients. A&A **587**, A61 (2016). `1510.08869`.

82. Heinke, C. O., Bahramian, A., Degenaar, N. & Wijnands, R. The nature of very faint X-ray binaries: hints from light curves. MNRAS **447**, 3034–3043 (2015). `1412.4097`.

83. Wilson, J. C. *et al.* A Wide-Field Infrared Camera for the Palomar 200-inch Telescope. In Iye, M. & Moorwood, A. F. M. (eds.) *Instrument Design and Performance for Optical/Infrared Ground-based Telescopes*, vol. 4841 of *Proceedings of SPIE*, 451–458 (2003).

84. McGregor, P. *et al.* Gemini South Adaptive Optics Imager (GSAOI). In Moorwood, A. F. M. & Iye, M. (eds.) *Ground-based Instrumentation for Astronomy*, vol. 5492 of *Society of Photo-Optical Instrumentation Engineers (SPIE) Conference Series*, 1033–1044 (2004).

85. Carrasco, E. R. *et al.* Results from the commissioning of the Gemini South Adaptive Optics Imager (GSAOI) at Gemini South Observatory. In Ellerbroek, B. L., Marchetti, E. & Véran, J.-P. (eds.) *Adaptive Optics Systems III*, vol. 8447 of *Society of Photo-Optical Instrumentation Engineers (SPIE) Conference Series*, 84470N (2012).

86. Labrie, K., Anderson, K., Cárdenes, R., Simpson, C. & Turner, J. E. H. DRAGONS - Data Reduction for Astronomy from Gemini Observatory North and South. In Teuben, P. J., Pound, M. W., Thomas, B. A. & Warner, E. M. (eds.) *Astronomical Data Analysis Software and Systems XXVII*, vol. 523 of *Astronomical Society of the Pacific Conference Series*, 321 (2019).

87. Lang, D., Hogg, D. W. & Mykytyn, D. The Tractor: Probabilistic astronomical source detection and measurement. Astrophysics Source Code Library, record ascl:1604.008 (2016). `1604.008`.

88. Foreman-Mackey, D., Hogg, D. W., Lang, D. & Goodman, J. emcee: The MCMC Hammer. PASP **125**, 306 (2013). `1202.3665`.

89. Lawrence, A. *et al.* The UKIRT Infrared Deep Sky Survey (UKIDSS). MNRAS **379**, 1599–1617 (2007). `astro-ph/0604426`.

90. Oke, J. B. *et al.* The Keck Low-Resolution Imaging Spectrometer. PASP **107**, 375 (1995).

91. Herter, T. L. *et al.* The performance of TripleSpec at Palomar. In McLean, I. S. & Casali, M. M. (eds.) *Ground-based and Airborne Instrumentation for Astronomy II*, vol. 7014

of *Society of Photo-Optical Instrumentation Engineers (SPIE) Conference Series*, 70140X (2008).

92. Perley, D. A. Fully Automated Reduction of Longslit Spectroscopy with the Low Resolution Imaging Spectrometer at the Keck Observatory. PASP **131**, 084503 (2019). `1903.07629`.

93. Cushing, M. C., Vacca, W. D. & Rayner, J. T. Spextool: A Spectral Extraction Package for SpeX, a 0.8-5.5 Micron Cross-Dispersed Spectrograph. PASP **116**, 362–376 (2004).

94. Vacca, W. D., Cushing, M. C. & Rayner, J. T. A Method of Correcting Near-Infrared Spectra for Telluric Absorption. PASP **115**, 389–409 (2003). `astro-ph/0211255`.

95. Simcoe, R. A. *et al.* FIRE: a near-infrared cross-dispersed echellette spectrometer for the Magellan telescopes. In McLean, I. S. & Casali, M. M. (eds.) *Ground-based and Airborne Instrumentation for Astronomy II*, vol. 7014 of *Society of Photo-Optical Instrumentation Engineers (SPIE) Conference Series*, 70140U (2008).

96. Wilson, J. C. *et al.* Mass producing an efficient NIR spectrograph. In Moorwood, A. F. M. & Iye, M. (eds.) *Ground-based Instrumentation for Astronomy*, vol. 5492 of *Society of Photo-Optical Instrumentation Engineers (SPIE) Conference Series*, 1295–1305 (2004).

97. Prochaska, J. X. *et al.* Pypeit: The python spectroscopic data reduction pipeline. *Journal of Open Source Software* **5**, 2308 (2020). URL `https://doi.org/10.21105/joss.02308`.

98. Simcoe, R. A. *et al.* The FIRE infrared spectrometer at Magellan: construction and commissioning. In McLean, I. S., Ramsay, S. K. & Takami, H. (eds.) *Ground-based*

and Airborne Instrumentation for Astronomy III, vol. 7735 of *Society of Photo-Optical Instrumentation Engineers (SPIE) Conference Series*, 773514 (2010).

99. Tylenda, R. *et al.* V1309 Scorpii: merger of a contact binary. A&A **528**, A114 (2011). 1012.0163.

100. Tylenda, R. *et al.* OGLE-2002-BLG-360: from a gravitational microlensing candidate to an overlooked red transient. A&A **555**, A16 (2013). 1304.1694.

101. Crause, L. A. *et al.* The post-outburst photometric behaviour of V838 Mon. MNRAS **341**, 785–791 (2003). astro-ph/0301423.

102. MacLeod, M. *et al.* Lessons from the Onset of a Common Envelope Episode: the Remarkable M31 2015 Luminous Red Nova Outburst. ApJ **835**, 282 (2017). 1605.01493.

103. Blagorodnova, N. *et al.* Progenitor, precursor, and evolution of the dusty remnant of the stellar merger M31-LRN-2015. MNRAS **496**, 5503–5517 (2020). 2004.04757.

104. Pastorello, A. *et al.* Forbidden hugs in pandemic times. I. Luminous red nova AT 2019zhd, a new merger in M 31. A&A **646**, A119 (2021). 2011.10588.

105. Pastorello, A. *et al.* Luminous red novae: Stellar mergers or giant eruptions? A&A **630**, A75 (2019). 1906.00812.

106. Pastorello, A. *et al.* The evolution of luminous red nova AT 2017jfs in NGC 4470. A&A **625**, L8 (2019). 1906.00811.

107. Cai, Y. Z. *et al.* The transitional gap transient AT 2018hso: new insights into the luminous red nova phenomenon. A&A **632**, L6 (2019). 1909.13147.

108. Pastorello, A. *et al.* Forbidden hugs in pandemic times. II. The luminous red nova variety: AT 2020hat and AT 2020kog. A&A **647**, A93 (2021). 2011.10590.

109. Blagorodnova, N. *et al.* The luminous red nova AT 2018bwo in NGC 45 and its binary yellow supergiant progenitor. A&A **653**, A134 (2021). 2102.05662.

110. Han, Z. *et al.* Spectroscopic properties of the dwarf nova-type cataclysmic variables observed by LAMOST. PASJ **72**, 76 (2020). 2007.14016.

111. Hillenbrand, L. A. *et al.* Gaia 17bpi: An FU Ori-type Outburst. ApJ **869**, 146 (2018). 1812.06640.

112. Hodapp, K. W. *et al.* The New EXor Outburst of ESO-Hα 99 Observed by Gaia ATLAS and TESS. AJ **158**, 241 (2019). 1909.10636.

113. Herczeg, G. J. *et al.* The Eruption of the Candidate Young Star ASASSN-15QI. ApJ **831**, 133 (2016). 1607.06368.

114. Ramsey, L. W. Observations of the TiO 8860 band in M giants. AJ **86**, 557–560 (1981).

115. Kenyon, S. J. & Fernandez-Castro, T. The Cool Components of Symbiotic Stars. I. Optical Spectral Types. AJ **93**, 938 (1987).

116. Gonneau, A. *et al.* The X-shooter Spectral Library (XSL): Data release 2. A&A **634**, A133 (2020). 2001.03080.

117. Fitzpatrick, E. L. Correcting for the Effects of Interstellar Extinction. PASP **111**, 63–75 (1999). astro-ph/9809387.

118. Ramirez, S. V., Depoy, D. L., Frogel, J. A., Sellgren, K. & Blum, R. D. Luminosity and Temperature from Near-Infrared Spectra of Late-Type Giant Stars. AJ **113**, 1411–1420 (1997).

119. Patat, F. *et al.* Detection of Circumstellar Material in a Normal Type Ia Supernova. *Science* **317**, 924 (2007). 0707.2793.

120. Wang, X. *et al.* The Cold and Dusty Circumstellar Matter around Fast-expanding Type Ia Supernovae. ApJ **882**, 120 (2019). 1810.11936.

121. Cai, Y. Z. *et al.* Observations of the luminous red nova AT 2021biy in the nearby galaxy NGC 4631. *arXiv e-prints* arXiv:2207.00734 (2022). 2207.00734.

122. Munari, U. & Zwitter, T. Equivalent width of NA I and K I lines and reddening. A&A **318**, 269–274 (1997).

123. Starrfield, S., Iliadis, C. & Hix, W. R. The Thermonuclear Runaway and the Classical Nova Outburst. PASP **128**, 051001 (2016). 1605.04294.

124. Hartmann, L. & Kenyon, S. J. The FU Orionis Phenomenon. ARA&A **34**, 207–240 (1996).

125. Hartmann, L., Herczeg, G. & Calvet, N. Accretion onto Pre-Main-Sequence Stars. ARA&A **54**, 135–180 (2016).

126. Fischer, W. J. *et al.* Accretion Variability as a Guide to Stellar Mass Assembly. *arXiv e-prints* arXiv:2203.11257 (2022). 2203.11257.

127. Sicilia-Aguilar, A. *et al.* Accretion dynamics of EX Lupi in quiescence. The star, the spot, and the accretion column. A&A **580**, A82 (2015). 1505.08011.

128. Blagorodnova, N. *et al.* Common Envelope Ejection for a Luminous Red Nova in M101. ApJ **834**, 107 (2017). 1607.08248.

129. Rayner, J. T., Cushing, M. C. & Vacca, W. D. The Infrared Telescope Facility (IRTF) Spectral Library: Cool Stars. ApJS **185**, 289–432 (2009). 0909.0818.

130. Rushton, M. T. *et al.* Spectral evolution of V838 Monocerotis in the optical and near-infrared in early 2002. MNRAS **360**, 1281–1289 (2005).

131. Loebman, S. R. *et al.* The Continued Optical to Mid-Infrared Evolution of V838 Monocerotis. AJ **149**, 17 (2015). 1409.2513.

132. Ivezic, Z. & Elitzur, M. Self-similarity and scaling behaviour of infrared emission from radiatively heated dust - I. Theory. MNRAS **287**, 799–811 (1997). astro-ph/9612164.

133. Ivezic, Z., Nenkova, M. & Elitzur, M. User Manual for DUSTY. *arXiv e-prints* astro–ph/9910475 (1999). astro-ph/9910475.

134. Ossenkopf, V., Henning, T. & Mathis, J. S. Constraints on cosmic silicates. A&A **261**, 567–578 (1992).

135. Mathis, J. S., Rumpl, W. & Nordsieck, K. H. The size distribution of interstellar grains. ApJ **217**, 425–433 (1977).

136. De, K. *et al.* SRGA J181414.6-225604: A new Galactic symbiotic X-ray binary outburst triggered by an intense mass loss episode of a heavily obscured Mira variable. *arXiv e-prints* arXiv:2205.09139 (2022). 2205.09139.

137. Tylenda, R. & Kamiński, T. Evolution of the stellar-merger red nova V1309 Scorpii: Spectral energy distribution analysis. A&A **592**, A134 (2016). 1606.09426.

138. Iaconi, R., Maeda, K., Nozawa, T., De Marco, O. & Reichardt, T. Properties of the post in-spiral common envelope ejecta II: dust formation. MNRAS **497**, 3166–3179 (2020). 2003.06151.

139. Drimmel, R., Cabrera-Lavers, A. & López-Corredoira, M. A three-dimensional Galactic extinction model. A&A **409**, 205–215 (2003). astro-ph/0307273.

140. Marshall, D. J., Robin, A. C., Reylé, C., Schultheis, M. & Picaud, S. Modelling the Galactic interstellar extinction distribution in three dimensions. A&A **453**, 635–651 (2006). astro-ph/0604427.

141. Green, G. M., Schlafly, E., Zucker, C., Speagle, J. S. & Finkbeiner, D. A 3D Dust Map Based on Gaia, Pan-STARRS 1, and 2MASS. ApJ **887**, 93 (2019). 1905.02734.

142. Bovy, J., Rix, H.-W., Green, G. M., Schlafly, E. F. & Finkbeiner, D. P. On Galactic Density Modeling in the Presence of Dust Extinction. ApJ **818**, 130 (2016). 1509.06751.

143. Matsumoto, T. & Metzger, B. D. Light Curve Model for Luminous Red Novae and Inferences about the Ejecta of Stellar Mergers. *arXiv e-prints* arXiv:2202.10478 (2022). 2202.10478.

144. Tylenda, R., Crause, L. A., Górny, S. K. & Schmidt, M. R. V4332 Sagittarii revisited. A&A **439**, 651–661 (2005). astro-ph/0412205.

145. Valenti, S. *et al.* The diversity of Type II supernova versus the similarity in their progenitors. MNRAS **459**, 3939–3962 (2016). 1603.08953.

146. Choi, J. *et al.* Mesa Isochrones and Stellar Tracks (MIST). I. Solar-scaled Models. ApJ **823**, 102 (2016). 1604.08592.

147. Hut, P. Tidal evolution in close binary systems. A&A **99**, 126–140 (1981).

148. Mardling, R. A. & Lin, D. N. C. Calculating the Tidal, Spin, and Dynamical Evolution of Extrasolar Planetary Systems. ApJ **573**, 829–844 (2002).

149. Levrard, B., Winisdoerffer, C. & Chabrier, G. Falling Transiting Extrasolar Giant Planets. ApJ **692**, L9–L13 (2009). 0901.2048.

150. Laor, A. & Draine, B. T. Spectroscopic Constraints on the Properties of Dust in Active Galactic Nuclei. ApJ **402**, 441 (1993).

151. Pejcha, O. Burying a Binary: Dynamical Mass Loss and a Continuous Optically thick Outflow Explain the Candidate Stellar Merger V1309 Scorpii. ApJ **788**, 22 (2014). 1307.4088.

152. Pejcha, O., Metzger, B. D., Tyles, J. G. & Tomida, K. Pre-explosion Spiral Mass Loss of a Binary Star Merger. ApJ **850**, 59 (2017). 1710.02533.

153. Munari, U. *et al.* The mysterious eruption of V838 Mon. A&A **389**, L51–L56 (2002). astro-ph/0205288.

154. De, K. *et al.* The Zwicky Transient Facility Census of the Local Universe. I. Systematic Search for Calcium-rich Gap Transients Reveals Three Related Spectroscopic Subclasses. ApJ **905**, 58 (2020). 2004.09029.

155. Cautun, M. *et al.* The milky way total mass profile as inferred from Gaia DR2. MNRAS **494**, 4291–4313 (2020). 1911.04557.

156. Nandez, J. L. A., Ivanova, N. & Lombardi, J., J. C. V1309 Sco—Understanding a Merger. ApJ **786**, 39 (2014). 1311.6522.

157. Zhu, L.-Y., Zhao, E.-G. & Zhou, X. A low-mass-ratio and deep contact binary as the progenitor of the merger V1309 Sco. *Research in Astronomy and Astrophysics* **16**, 68 (2016). 1611.04699.

158. MacLeod, M., Cantiello, M. & Soares-Furtado, M. Planetary Engulfment in the Hertzsprung-Russell Diagram. ApJ **853**, L1 (2018). 1801.04274.

159. Metzger, B. D., Giannios, D. & Spiegel, D. S. Optical and X-ray transients from planet-star mergers. MNRAS **425**, 2778–2798 (2012). 1204.0796.

160. Jackson, B. & Carlberg, J. Accretion of Planetary Material onto Host Stars. In Deeg, H. J. & Belmonte, J. A. (eds.) *Handbook of Exoplanets*, 28 (2018).

161. MacLeod, M. & Loeb, A. Runaway Coalescence of Pre-common-envelope Stellar Binaries. ApJ **893**, 106 (2020). 1912.05545.

162. MacLeod, M., De, K. & Loeb, A. Dusty, Self-Obscured Transients from Stellar Mergers and Common Envelope Phases. *arXiv e-prints* arXiv:2205.07929 (2022). 2205.07929.

163. MacLeod, M. morganemacleod/RLOF: v1.1. Zenodo (2020).

164. MacLeod, M. & Loeb, A. Pre-common-envelope Mass Loss from Coalescing Binary Systems. ApJ **895**, 29 (2020). 2003.01123.

165. MacLeod, M., Ostriker, E. C. & Stone, J. M. Bound Outflows, Unbound Ejecta, and the Shaping of Bipolar Remnants during Stellar Coalescence. ApJ **868**, 136 (2018). 1808.05950.

166. Kamiński, T. *et al.* Submillimeter-wave emission of three Galactic red novae: cool molecular outflows produced by stellar mergers. A&A **617**, A129 (2018). 1804.01610.

167. Claussen, M. J., Bond, H. E., Starrfield, S. & Healy, K. Variable SiO Maser Emission from V838 Monocerotis. In *ASP*, vol. 363, 87 (2007).

168. Ortiz-León, G. N. *et al.* SiO maser astrometry of the red transient V838 Monocerotis. A&A **638**, A17 (2020). 2004.01488.

169. Winn, J. N. & Fabrycky, D. C. The Occurrence and Architecture of Exoplanetary Systems. ARA&A **53**, 409–447 (2015). 1410.4199.

170. Rasio, F. A., Tout, C. A., Lubow, S. H. & Livio, M. Tidal Decay of Close Planetary Orbits. ApJ **470**, 1187 (1996). astro-ph/9605059.

171. Popkov, A. V. & Popov, S. B. The rate of planet-star coalescences due to tides and stellar evolution. MNRAS **490**, 2390–2404 (2019). 1909.01719.

172. Patra, K. C. *et al.* The Continuing Search for Evidence of Tidal Orbital Decay of Hot Jupiters. AJ **159**, 150 (2020). 2002.02606.

173. Yee, S. W. *et al.* The Orbit of WASP-12b Is Decaying. ApJ **888**, L5 (2020). 1911.09131.

174. McMillan, P. J. Mass models of the Milky Way. MNRAS **414**, 2446–2457 (2011). 1102.4340.

175. Beleznay, M. & Kunimoto, M. Exploring the dependence of hot Jupiter occurrence rates on stellar mass with TESS. MNRAS **516**, 75–83 (2022). 2207.12522.

176. Stephan, A. P., Naoz, S. & Gaudi, B. S. A-type Stars, the Destroyers of Worlds: The Lives and Deaths of Jupiters in Evolving Stellar Binaries. AJ **156**, 128 (2018). 1806.04145.

177. Staff, J. E., De Marco, O., Wood, P., Galaviz, P. & Passy, J.-C. Hydrodynamic simulations of the interaction between giant stars and planets. MNRAS **458**, 832–844 (2016). 1602.03130.

178. Yamazaki, R., Hayasaki, K. & Loeb, A. Optical-infrared flares and radio afterglows by Jovian planets inspiraling into their host stars. MNRAS **466**, 1421–1427 (2017). 1512.01747.

179. Gurevich, O., Bear, E. & Soker, N. Faint intermediate luminosity optical transients (ILOTs) from engulfing exoplanets on the Hertzsprung gap. MNRAS **511**, 1330–1335 (2022). 2111.06317.

180. Stephan, A. P., Naoz, S., Gaudi, B. S. & Salas, J. M. Eating Planets for Lunch and Dinner: Signatures of Planet Consumption by Evolving Stars. ApJ **889**, 45 (2020). 1909.05259.

181. Soares-Furtado, M., Cantiello, M., MacLeod, M. & Ness, M. K. Lithium Enrichment Signatures of Planetary Engulfment Events in Evolved Stars. AJ **162**, 273 (2021). 2002.05275.

182. Spina, L. *et al.* Chemical evidence for planetary ingestion in a quarter of Sun-like stars. *Nature Astronomy* **5**, 1163–1169 (2021). 2108.12040.

183. Metzger, B. D., Shen, K. J. & Stone, N. Secular dimming of KIC 8462852 following its consumption of a planet. MNRAS **468**, 4399–4407 (2017). 1612.07332.

184. Siess, L. & Livio, M. The accretion of brown dwarfs and planets by giant stars - I. Asymptotic giant branch stars. MNRAS **304**, 925–937 (1999). astro-ph/9812220.

185. Israelian, G., Santos, N. C., Mayor, M. & Rebolo, R. Lithium in stars with exoplanets. A&A **414**, 601–611 (2004). astro-ph/0310378.

186. Kamiński, T. *et al.* Lithium in coalesced non-compact stars. *arXiv e-prints* arXiv:2207.06779 (2022). 2207.06779.

187. Carlberg, J. K., Majewski, S. R. & Arras, P. The Role of Planet Accretion in Creating the Next Generation of Red Giant Rapid Rotators. ApJ **700**, 832–843 (2009). 0906.1587.

188. Zhang, M. & Penev, K. Stars Get Dizzy After Lunch. ApJ **787**, 131 (2014). 1404.4365.

189. Aguilera-Gómez, C., Chanamé, J., Pinsonneault, M. H. & Carlberg, J. K. On Lithium-rich Red Giants. I. Engulfment of Substellar Companions. ApJ **829**, 127 (2016). 1605.05332.

Table 1: Photometry of ZTF SLRN-2020 in the optical and IR bands (continued).

MJD	Phase (d)	Filter	Mag	Instrument
59144.21	149.82	o	19.57 ± 0.17	ATLAS
59148.22	153.83	o	> 18.39	ATLAS
59154.24	159.85	o	19.49 ± 0.10	ATLAS
59158.19	163.80	o	19.53 ± 0.17	ATLAS
59164.23	169.84	o	19.44 ± 0.12	ATLAS
59184.19	189.80	o	19.49 ± 0.16	ATLAS

Table 2: Template-subtracted NEOWISE mid-IR photometry of ZTF SLRN-2020.

MJD	Phase days	Filter	Flux mJy
55296.47	-3697.92	$W1$	0.16 ± 0.11
55479.51	-3514.88	$W1$	0.00 ± 0.08
56940.99	-2053.40	$W1$	-0.12 ± 0.13
57122.03	-1872.36	$W1$	0.11 ± 0.21
57300.01	-1694.38	$W1$	-0.02 ± 0.14
57487.55	-1506.84	$W1$	0.02 ± 0.21
57658.98	-1335.41	$W1$	-0.08 ± 0.14
57851.76	-1142.63	$W1$	-0.09 ± 0.19
58021.99	-972.40	$W1$	-0.07 ± 0.12
58217.44	-776.95	$W1$	0.02 ± 0.22
58381.60	-612.79	$W1$	-0.13 ± 0.13
58583.15	-411.24	$W1$	0.02 ± 0.22
58747.25	-247.14	$W1$	0.07 ± 0.14
58949.95	-44.44	$W1$	0.26 ± 0.22
59113.93	119.54	$W1$	2.21 ± 0.13
59314.32	319.93	$W1$	1.03 ± 0.23
59478.41	484.02	$W1$	0.42 ± 0.12
55296.47	-3697.92	$W2$	0.03 ± 0.09

Table 2: Template-subtracted NEOWISE mid-IR photometry of ZTF SLRN-2020 (continued).

MJD	Phase days	Filter	Flux mJy
55479.51	-3514.88	$W2$	0.03 ± 0.08
56940.99	-2053.40	$W2$	-0.12 ± 0.09
57122.03	-1872.36	$W2$	0.00 ± 0.10
57300.01	-1694.38	$W2$	-0.16 ± 0.10
57487.55	-1506.84	$W2$	-0.12 ± 0.11
57658.98	-1335.41	$W2$	-0.12 ± 0.09
57851.69	-1142.70	$W2$	-0.09 ± 0.11
58021.99	-972.40	$W2$	-0.01 ± 0.10
58217.44	-776.95	$W2$	0.00 ± 0.10
58381.60	-612.79	$W2$	-0.15 ± 0.11
58583.15	-411.24	$W2$	0.01 ± 0.13
58747.25	-247.14	$W2$	0.13 ± 0.10
58949.88	-44.51	$W2$	0.47 ± 0.12
59113.93	119.54	$W2$	2.60 ± 0.11
59314.32	319.93	$W2$	1.12 ± 0.13
59478.41	484.02	$W2$	0.40 ± 0.12

Table 3: Archival photometry of the progenitor of ZTF SLRN-2020 along with the time of observation. Upper limits are reported at 5σ confidence.

Survey	MJD	Filter	Mag
UKIRT	54340.36	J	> 17.50
	54340.37	H	16.66 ± 0.25
	54997.52	K	16.32 ± 0.18
PS1	55744.48	g	> 22.03
	55806.58	r	> 22.02
	55813.56	i	> 21.82
	55925.06	z	> 20.97
	56179.10	y	> 19.93

Table 4: Spectroscopic follow-up of ZTF SLRN-2020. The spectra denoted by † were stacked together to obtain the final binned late-time NIR spectrum.

Date	Phase	Instrument	Exposure time	Wavelength Range	Resolution
UT	d		s	Å	
2020-10-29	+156	P200 + TSpec	1200	$10000 - 24500$	≈ 2700
2020-11-20	+178	Keck-I + LRIS	1200	$3200 - 10000$	≈ 1000
2022-03-17†	+660	Keck-II + NIRES	2400	$10000 - 24500$	≈ 2700
2022-04-03†	+677	Magellan/Baade + FIRE/Echelle	3600	$9000 - 25000$	≈ 6000
2022-05-25†	+729	Magellan/Baade + FIRE/Prism	3000	$9000 - 25000$	$\approx 300 - 500$

Table 5: Derived dust parameters from the multi-epoch `DUSTY` modeling of ZTF SLRN-2020. The radius inner shell and ejecta mass are derived for an estimated distance of 4 kpc.

Phase	F	τ	A_V	T_*	T_d	r_{in}	M_{ej}
d	10^{-12} erg cm^{-2} s^{-1}	($\lambda = 0.55\,\mu$m)	mag	K	K	AU	M$_\odot$
+120	$10.0^{+3.2}_{-1.9}$	$1.8^{+0.8}_{-0.7}$	$3.6^{+0.6}_{-0.7}$	8970^{+508}_{-390}	1014^{+84}_{-73}	$1.3^{+0.2}_{-0.1}$	$8.8^{+1.7}_{-1.6} \times 10^{-8}$
+320	$11.5^{+17.9}_{-6.5}$	$13.0^{+3.4}_{-5.7}$	3.6 (fixed)	4300^{+1850}_{-1230}	415^{+143}_{-76}	$5.3^{+3.2}_{-1.8}$	$10.2^{+22.7}_{-7.7} \times 10^{-7}$